Title
Regulation of Southwestern United States Precipitation by non-ENSO Teleconnections and the Impact of the Background Flow

Journal
Journal of Climate, 36(21)

ISSN
0894-8755

Authors
Dong, Cameron
Peings, Yannick
Magnusdottir, Gudrun

Publication Date
2023-11-01

DOI
10.1175/jcli-d-23-0081.1

Peer reviewed

Regulation of Southwestern United States Precipitation by non-ENSO Teleconnections and the Impact of the Background Flow

Cameron Dong,[a] Yannick Peings,[a] Gudrun Magnusdottir[a]

[a] *Department of Earth System Science, University of California Irvine, Irvine, CA 92697, USA*

Corresponding author: Cameron Dong, cmdong@uci.edu

ABSTRACT

In this study, we analyze drivers of non-El Niño Southern Oscillation (ENSO) precipitation variability in the Southwest United States (SWUS) and the influence of the atmospheric basic state, using atmosphere-only and ocean-atmosphere coupled simulations from the Community Earth System Model version 2 (CESM2) large ensemble. A cluster analysis identifies three main wavetrains associated with non-ENSO SWUS precipitation in the experiments: a meridional ENSO-type wavetrain, an arching Pacific North American-type (PNA) wavetrain, and a circumglobal zonal wavetrain. The zonal wavetrain cluster frequency differs between models and ENSO phase, with decreased frequency during El Niño and the coupled runs, and increased frequency during La Niña and the atmosphere-only runs. This is consistent with an El Niño-like bias of the atmospheric circulation in the coupled model, with strengthened subtropical westerlies in the central and eastern North Pacific that cause a retraction of the waveguide in the midlatitude eastern North Pacific. As such, zonal wavetrains from the East Asian Jet Stream (EAJS) are more likely to be diverted southward in the East Pacific in the coupled large ensemble, with a consequently smaller role in driving SWUS precipitation variability. This study illustrates the need to reduce model biases in the background flow, particularly relating to the jet stream, in order to accurately capture the role of large-scale teleconnections in driving SWUS variability and improve future forecasting capabilities.

1. Introduction

One of the greatest scientific challenges in the field of atmospheric dynamics is providing skillful climate/weather predictions beyond the traditional two-week time horizon and into the subseasonal to seasonal (S2S) range (Vitart et al. 2017). This challenge is particularly notable for precipitation prediction in the SWUS, which is plagued by low prediction skill compared to other regions (Kumar and Chen 2020, Roy et al. 2020, Becker et al. 2022). In addition, the region contains the most populous and agriculturally productive state in the United States, California. As a result, improved prediction of precipitation is of utmost importance for local, state, and federal bodies to properly allocate and manage limited water resources in the SWUS (e.g., Sengupta et al. 2022).

The importance of improved prediction has been especially illustrated by the recent persistent multi-year drought in the region (Seager and Henderson 2016, Swain et al. 2014, Swain 2015). As of 2016, it was estimated to have resulted in billions of dollars in economic losses as well as shortages of water for rural consumption, agriculture, hydroelectric power, and other usages (Lund et al. 2018). However, despite numerous studies over the past decade analyzing the mechanisms regulating SWUS precipitation, there is little consensus regarding the drivers of the drought-inducing atmospheric circulation, and there are many gaps to fill regarding our understanding of SWUS precipitation variability.

In this study, we are primarily concerned with large-scale atmospheric patterns and teleconnections that regulate SWUS precipitation. Although SWUS precipitation is brought by midlatitude cyclones and associated atmospheric rivers (ARs) that form over the northern Pacific Ocean during boreal winter (Ralph and Dettinger 2011, Dettinger 2013, Rutz et al. 2014, Payne and Magnusdottir 2014), known limits in atmospheric predictability (Lorenz 1963) make it impossible to predict individual storms and ARs on S2S timescales. Despite this, there may still be potential to predict the large-scale atmospheric circulation pattern that regulates AR landfall and frequency (e.g., DeFlorio et al. 2019). AR landfall and SWUS precipitation anomalies are strongly associated with the presence of trough or ridge conditions in the midlatitude Eastern North Pacific (ENP). A trough results in a strengthened subtropical East Pacific jet, which guides more storms and ARs toward the SWUS, while a ridge is associated with a weakened subtropical jet and decreased storm and AR activity in the SWUS (e.g., Gibson et al. 2020, Mundhenk et al. 2016, Swain et al. 2017, Teng and Branstator 2017, Payne and Magnusdottir 2016). Therefore, identifying the dominant S2S drivers of trough or ridge conditions in the ENP provides a path for improving SWUS precipitation prediction and areas to focus future model development.

Traditionally, ENSO has been the primary tool for SWUS precipitation prediction on seasonal (and to a lesser extent subseasonal) timescales. This is because of its large effect on the Northern Hemisphere atmospheric circulation during boreal winter and its slow evolution on seasonal timescales. During an average El Niño, Eastern tropical Pacific warm SST anomalies drive deep convection that leads to the propagation of Rossby waves to the midlatitudes (Hoskins and Karoly 1981), resulting in an extension of the Northern subtropical Pacific jet and wet conditions in the SWUS (Trenberth 1997, Horel and Wallace 1981, Ropelewski and Halbert 1986, L'Heureux et al. 2015, Deser et al. 2018). During an average La Niña, the opposite occurs, with a weakening of the jet and dry conditions in the SWUS.

However, the ENSO-SWUS precipitation relationship is dependent on the spatial and temporal evolution of SST's (Lee et al. 2018, Patricola et al. 2020), can be dominated by noise (Kumar and Chen 2020, Zhang et al. 2018, Swenson et al. 2019), and may vary nonlinearly with ENSO strength (Jong et al. 2016, Garfinkel et al. 2019). Therefore, the observed ENSO response in any particular period can deviate significantly from the composite ENSO response. Notably, the teleconnection has appeared weaker during the recent decade and persistent drought conditions (Lee et al. 2018). The water years 2013-14 and 2014-15 (defined as a November through March season) experienced severe drought conditions, despite neutral and weakly positive ENSO conditions, respectively. The following historically strong 2015-16 El Niño only resulted in average SWUS rain, followed by the region unexpectedly experiencing a brief respite during the ENSO-neutral 2016-17 deluge (Wang et al. 2017). Clearly, the ENSO state has not been sufficient to provide skillful predictions of SWUS precipitation during this time period, and it is necessary to find non-ENSO drivers of precipitation that can provide additional predictive skill.

There are many potential non-ENSO drivers of SWUS precipitation that researchers have explored. First, these include non-ENSO SST variability, such as Western Pacific tropical SST (Hartmann 2015, Seager and Henderson 2016, Watson et al. 2016, Lee et al. 2015) and Indian Ocean SST (Siler et al. 2017, Seager and Henderson 2016), as well as sea ice concentration variability (Cohen et al. 2017, Lee et al. 2015), all of which may drive midlatitude circulation responses. Additionally, there may be a role for the Madden Julian Oscillation (MJO), due to its slow eastward propagation of organized tropical convection with a semi-regular period of 30-90 days (Zhang 2005). The MJO has been found to excite different midlatitude circulation patterns depending on its phase (Arcodia et al. 2020, Moon et al. 2011, Riddle et al. 2013, Roundy et al. 2010), and it plays a role for subseasonal prediction (Mundhenk et al. 2018, Henderson et al. 2016, Stan et al. 2022, Lim et al. 2021) and potentially even seasonal prediction (Peng et al. 2019, Peings et al. 2022). Lastly, there are teleconnection patterns associated with internal midlatitude atmospheric dynamics, which may be intrinsic modes of the atmosphere that may also be excited by outside forcing. The most prominent of these teleconnections include the PNA pattern (Li et al. 2019, Lopez and Kirtman 2019) and the circumglobal teleconnection patterns (CGT's; Branstator 2002, Branstator and Teng 2017, Hoskins and Ambrizzi 1993), which are associated with Rossby wavetrains guided by the jet stream that can set up trough or ridge conditions in the ENP (Teng and Branstator 2017).

Although many potential non-ENSO teleconnections have been explored, and there are indications that including these non-ENSO drivers can lead to improved predictions (e.g., through machine learning; Gibson et al. 2021), there is still a long way to go in providing skillful S2S predictions of SWUS precipitation. In addition, there is still a need to explore how non-ENSO SWUS precipitation variability can vary depending on the ENSO state and model choice. ENSO may modulate the tropical mean state that regulates tropical convective variability (e.g., MJO intensity and propagation; Liu et al. 2016, Kang et al. 2021) as well as the extratropical atmospheric background flow that is instrumental for Rossby wave propagation and breaking. Similarly, different model setups introduce their own unique biases in the mean state, feedbacks, and model physics and parameterizations that may influence SWUS teleconnection variability. Recent studies show that even in S2S forecasting, mean state biases quickly emerge after initialization (Garfinkel et al. 2022). In addition, there may be large differences in tropical convective variability between atmospheric models often used in hindcast experiments and coupled models typically used in forecasting (e.g., MJO propagation; Woolnough et al. 2007, DeMott et al. 2019), as well as between models and observations.

Due to these issues, we supplement our analysis of observations and reanalysis data with the fully coupled CESM2 large ensemble experiment (Rodgers et al. 2021) and the atmosphere-only CESM2 Atmospheric Model Intercomparison Project (AMIP) experiment (NCAR Climate Variability and Change Working Group). This allows for a robust assessment and reduction of the influence of internal variability in statistical analyses for studying how a state-of-the-art climate model represents the key teleconnections that influence SWUS rainfall, during different ENSO states, as well as with either a freely evolving ocean or with prescribed observational SST. During our analysis of the model experiments and observational and reanalysis dataset, we aim to answer the following major questions with regards to subseasonal monthly variability of SWUS precipitation:

1. What are the dominant non-ENSO teleconnection patterns that interfere with the expected ENSO-SWUS precipitation teleconnection?
2. How do the different teleconnections interact with the ENSO basic state?
3. How well are these teleconnections represented in models, and how might that affect SWUS precipitation prediction?

Section 2 presents the data and methodology used. Section 3 describes results from our analyses, and Section 4 contains the conclusions and a discussion of the main findings.

2. Data and Diagnostics

a. Observational and Reanalysis Data

For historical global atmospheric variables, we use monthly data from the ERA5 global reanalysis product (Hersbach et al. 2020), which uses a data assimilation system to constrain observations from 1940-present with a horizontal spatial resolution of 31 km and 137 vertical levels. We use historical SST from the Extended Reconstructed Sea Surface Temperature version 5 (ERSSTv5) dataset, which is a monthly global sea surface temperature dataset derived from the International Comprehensive Ocean-Atmosphere Dataset (ICOADS) Release 3.0, with data from 1854 to present on a 2.0° by 2.0° grid. Historical precipitation over the United States is taken from the Climate Prediction Center (CPC) monthly rain gauge data set over the years 1948-present on a 0.25° by 0.25° grid.

b. Model Experiment Data

The model data comes from two experiments running CESM2. The first set of simulations is the CESM2 large ensemble (LENS2; Rodgers et al. 2021), which uses the fully coupled version. We use the first 50 ensemble members, which use the original Coupled Model Intercomparison Project 6 (CMIP6) biomass burning protocol and simulate the period 1850-2100 (Danabasoglu et al. 2020). The second set of simulations (GOGA) uses the atmosphere-only component of CESM2, the Community Atmosphere Model version 6 (CAM6), on a 1.25° by 0.9° horizontal grid with 32 vertical levels and a model top at 2.26 hPa. GOGA is a ten ensemble-member experiment where CAM6 is forced by prescribed global monthly SST from ERSSTv5 over the period 1880-2021, having been branched from the 11th LENS2 member on January 1st, 1880 through perturbations to the air temperature field.

c. Data Treatment and Climate Indices

Each dataset is trimmed to a common time interval, 1948-2020, which is also used to calculate climatological fields. Additionally, SST anomalies are calculated after first subtracting the global mean SST at each timestep to account for the global warming trend. All data are analyzed in either monthly or seasonal averages during NDJFM periods.

To represent ENSO, we use the Niño 3 index, calculated as the areal average of SST anomalies over the eastern tropical Pacific Ocean (210°E-270°E, 5°S-5°N). Analyses have also been tested using the Niño 3.4 index, which captures more central Pacific ENSO variability, but the results are similar. SWUS precipitation is calculated as an areal average over land within the box (235°E-251°E, 31°N-40°N). This region includes most of California, Nevada, Utah, and Arizona.

We perform linear regressions to measure and then remove the anomalies associated with ENSO, when analyzing non-ENSO mechanisms. This is performed individually at each grid point, such that for a variable X at latitude ϕ, longitude λ, and timestep i, the linear part of X dependent on ENSO is calculated as

$$X_{ENSO}^{\phi,\lambda,i} = a * ENSO_i + b$$

where a and b are constants derived from a simple linear regression between the ENSO 3 index and variable $X^{\phi,\lambda}$ over all timesteps i. Note that when calculated using variable anomalies, b is zero. Using this, we can also calculate "non-ENSO" anomalies by subtracting the linear ENSO anomalies from the total anomaly

$$X_{non-ENSO} = X - X_{ENSO}$$

where we have omitted the subscripts i, ϕ, and λ for simplicity. Analyses have also been performed using a quadratic least squares regression to account for the influence of nonlinear ENSO dependence, but results are similar and the main conclusions do not change.

d. Clustering Algorithm

The following analyses use an algorithm that places map patterns into separate clusters. Before clustering, we reduce the dimensionality of the data by using extended empirical orthogonal functions (EEOF's), where we select multiple variables, inputting the anomalies of these variables during selected timeframes and locations. For example, later analyses use monthly 200 hPa meridional wind and streamfunction anomalies during NDJFM months over a longitude-latitude box (180°E-260°E, 20°N-70°N). After this selection, we compute the first 20 EEOF's.

After computing the EEOF's, we perform the clustering using a Gaussian Mixture Model (GMM) algorithm from the Scikit-learn library in Python (Pedregosa et al. 2011). Each timestep is a sample data point with dimensionality equal to the number of selected EEOF's.

The clustering algorithm iteratively solves for *N* clusters from the data points, where *N* is a user-defined input, and each cluster is defined by a multivariate Gaussian probability distribution. Due to the possibility of local maxima, the clustering algorithm is randomly initiated 100 separate times. The highest scoring result is saved according to the Bayesian Information Criterion (BIC) score. After calculating the *N* clusters, each data point can be assigned to the cluster for which it has the highest probability (according to the multivariate Gaussian probability distributions).

Using a GMM has distinct advantages over the common clustering algorithm k-means, which can be formulated as a primitive version of the GMM expectation-maximization algorithm. While k-means has spherical distributions shapes, fixed partitions, and single cluster membership, GMM allows for elliptic distribution shapes, overlapping clusters, and probabilistic cluster membership. As such, GMM is more flexible and advantageous when analyzing monthly mean data that contains multiple overlapping atmospheric patterns.

e. Stationary Wavenumber of Rossby Waves

We use the 200 hPa mean flow to calculate the wavenumber for stationary Rossby waves from linear theory using a Mercator coordinate transform as in Hoskins and Ambrizzi (1993), where K_s is the stationary wavenumber, U is the zonal wind, a is the Earth's radius, ϕ is latitude, and β_M is the Mercator coordinate equivalent of the meridional gradient of absolute vorticity.

$$K_s = a\left(\frac{\beta_\mathrm{M}\cos\phi}{U}\right)^{1/2}$$

$$\beta_M = \left(2\Omega - \left(\frac{1}{\cos\phi}\frac{\partial}{\partial\phi}\right)^2 (U\cos\phi)\right)\frac{\cos^2\phi}{a^2}$$

We interpret the stationary wavenumber as follows. Under the assumption that locally the medium is varying only in the meridional direction, the zonal wavenumber k is constant, so that for each zonal wavenumber, the meridional wavenumber l can be deduced from the following: $K_s^2 = k^2 + l^2$. This implies that for stationary, linear Rossby wave solutions, a wave with zonal wavenumber k is restricted to regions of $K_s > k$, or else l will be imaginary and the waves will decay. Put another way, linear waves are refracted towards regions with higher K_s. Naturally, this places larger restrictions on short waves with higher zonal wavenumbers, particularly in waveguides along the jet streams. However, even larger scale waves with smaller wavenumbers will be refracted by the medium. While many of the assumptions of linear theory are not strictly valid, it can be useful for qualitative analysis.

3. Results

Our goal is to analyze non-ENSO mechanisms and how they regulate SWUS precipitation while interacting with ENSO. However, it is important to recognize that ENSO variability may differ between reanalysis, GOGA, and LENS2. This may impact the teleconnection strength between ENSO and SWUS precipitation, as well as how ENSO interacts with other non-ENSO mechanisms. In the first section we briefly compare ENSO tropical SST and convective variability, its induced large-scale atmospheric response, and the strength of the ENSO teleconnection with SWUS precipitation in each of the model experiments and reanalysis, before analyzing non-ENSO variability in the latter sections.

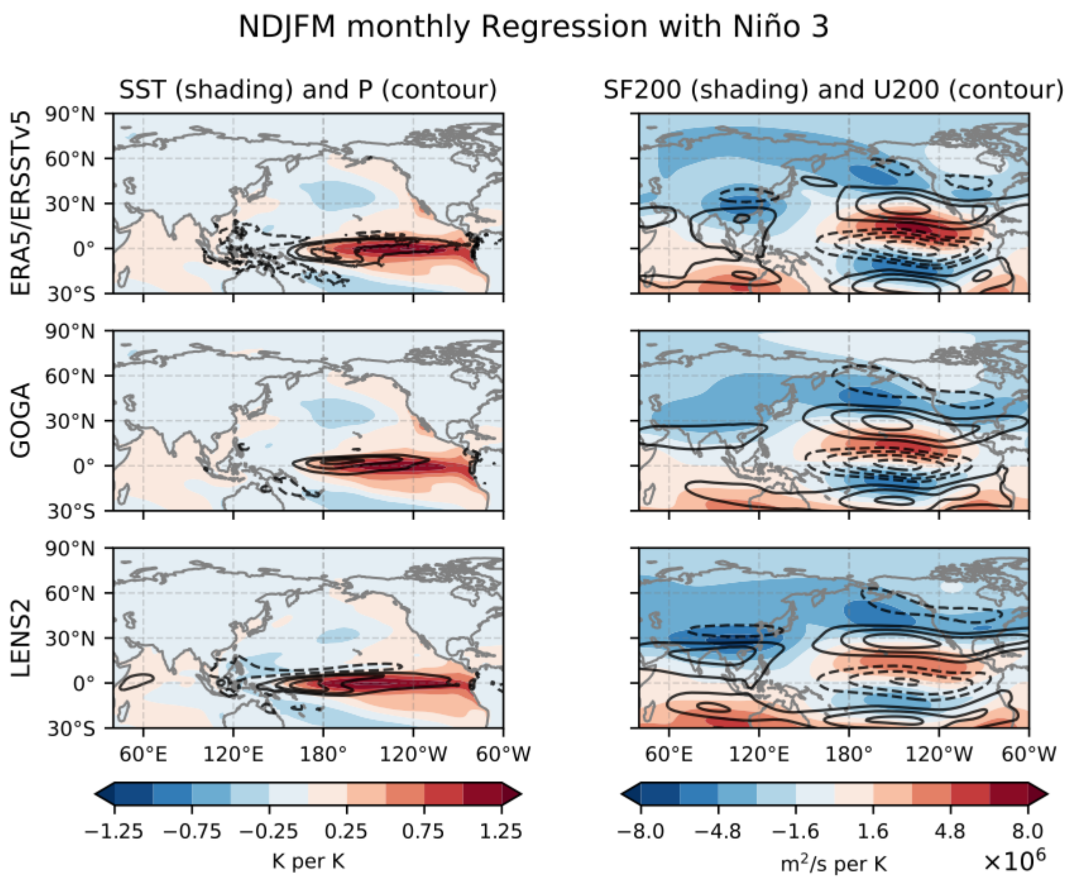

Fig. 1. Regression (left column) of monthly NDJFM SST (shading) and monthly NDJFM precipitation (contours) with the Niño 3 index in ERA5/ERSSTv5, GOGA and LENS2. Contour interval in left column is 1.0 mm day^{-1} K^{-1}, with zero contour omitted. Regression (right column) of monthly NDJFM SF200 (shading) and monthly NDJFM 200 hPa zonal wind (contours) with Niño 3 index in ERA5, GOGA, and LENS2. Contour interval in right column is 1.5 m s^{-1} K^{-1}, with zero contour omitted.

a. Comparison of model variability of the ENSO-SWUS precipitation teleconnection

In Figure 1, we display the regressed fields associated with the Niño 3 index during NDJFM months. The SST expression of ENSO (left column) is nearly identical between ERSSTv5 and GOGA, as expected due to the experimental design. However, in LENS2 there is a westward extension of the warm SST pool during El Niño as previously shown by Capotondi et al. (2020). As a result, the tropical atmospheric precipitation response is also shifted westward. However, this shift is not clearly manifested in a different ENSO extratropical response in LENS2, compared to GOGA and observations.

When comparing 200 hPa streamfunction (SF200) and 200 hPa zonal wind (U200), each dataset displays a similar meridional wavetrain in the central-eastern Pacific, which results in a trough in the extratropical North Pacific and strengthened subtropical North Pacific westerlies (Fig. 1 right panels). Calculating the longitude of maximum jet strengthening, we find that it occurs at 142.5° W in ERA5, 148.75° W in LENS2, and 155° W in GOGA. Thus, despite nearly identical monthly SST variability in GOGA and ERA5, there is about a 12° longitude westward shift in the jet strengthening maximum in GOGA. In contrast, despite a westward shift in warm tropical SST and convection in LENS2, the jet response maximum is shifted eastward relative to GOGA. This indicates that the zonal location of tropical warming and convection associated with ENSO is not necessarily a good predictor of small zonal shifts in the extratropical response, which could be important for SWUS precipitation prediction.

This concept is further elucidated when we construct regression maps with monthly NDJFM SWUS precipitation (Figure 2). While we might have initially expected a weaker ENSO-SWUS precipitation teleconnection in LENS2 due to the westward tropical convection shift (Patricola et al. 2020), this is clearly not the case. When analyzing the relationship between SWUS precipitation and tropical SST, it appears that GOGA has the weaker ENSO-SWUS rain relationship, in contrast to stronger relationships in LENS2 and ERA5/ERSSTv5, which exhibit stronger SST and precipitation signals in the ENSO region. Potentially, this may be related to the aforementioned shifts in the ENSO-induced jet response, where an eastward shift results in a stronger SWUS precipitation response. However, it is also important to remember that GOGA uses prescribed SST in the extratropics, so the lack of air-sea feedbacks may also weaken this relationship, such as by changing feedbacks in Rossby wave forcing or storm feedbacks.

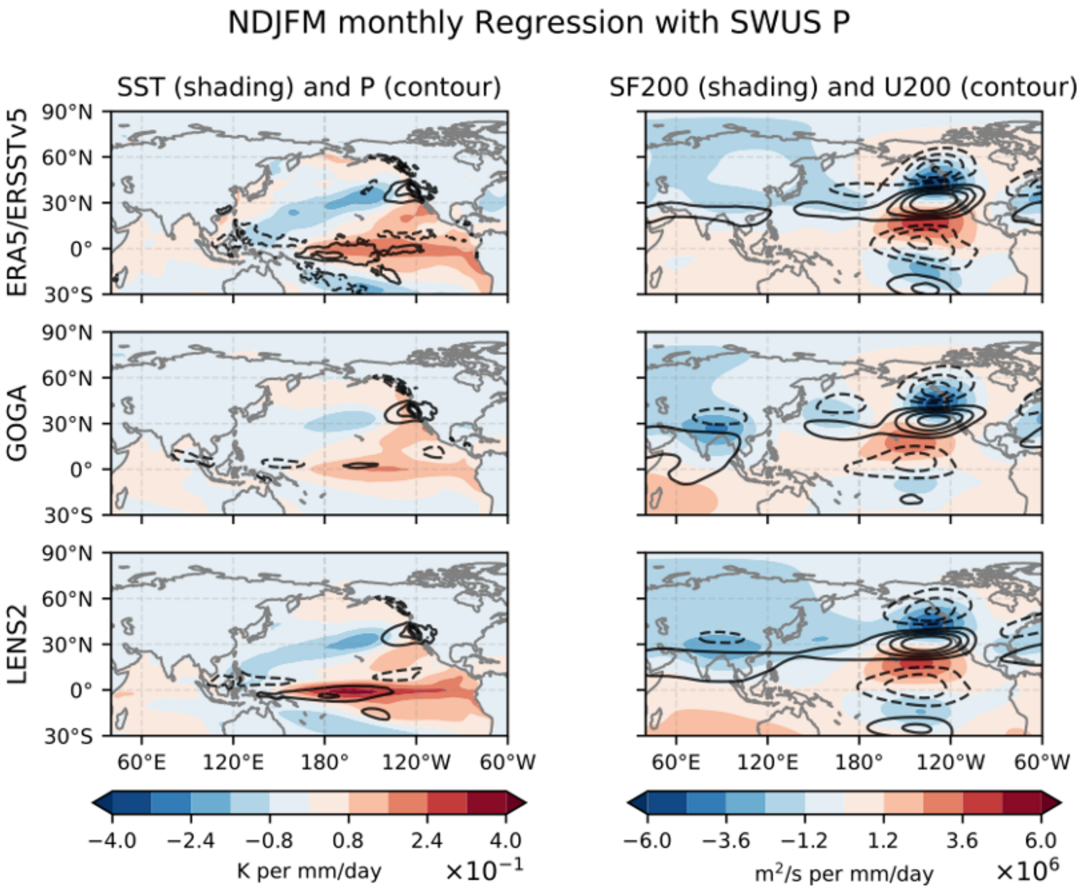

Fig. 2. Regression (left column) of NDJFM monthly SST (shading) and precipitation (contours) with SWUS precipitation in ERA5/ERSSTv5, GOGA and LENS2. Contour interval in left column is 0.5 mm day^{-1} per mm day^{-1}, with zero contour omitted. Regression (right column) of NDJFM monthly SF200 (shading) and U200 (contours) with SWUS precipitation in ERA5, GOGA, and LENS2. Contour interval in right column is 1.0 m s^{-1} per mm day^{-1}, with zero contour omitted.

When analyzing the SF200 and U200 patterns regressed with SWUS precipitation (Figure 2 right column), we identify similar patterns in the ENP in each dataset, with a trough and associated strengthened subtropical East Pacific westerlies. However, outside this region, there are numerous differences between GOGA, LENS2, and ERA5. Both LENS2 and ERA5 display significant signal from ENSO, with a meridional wavetrain in the central-eastern Pacific and strong negative zonal mean SF200 responses in the midlatitudes that resemble the ENSO regressed responses. In GOGA, there are also similarities to the regressed ENSO pattern, but the influence is weaker. GOGA exhibits stronger hints of a zonal pattern with troughs over East Asia, east of Japan, and in the ENP, which does not overlap with the ENSO regressed response. Similar patterns have been identified in previous studies, associated either with atmospheric internal variability or convection in the western tropical Pacific (Gibson et al. 2020, Swain et al. 2017, Teng and Branstator 2017).

As expected, ENSO is the dominant climate pattern associated with SWUS precipitation in each of ERA5, LENS2, and GOGA, although the connection appears weaker in GOGA. However, SWUS precipitation is highly variable, and ENSO only explains a small fraction of its variance. Figure 3 shows the correlation between the Niño 3 index and SWUS precipitation at monthly timescales, where it is under 0.2 for each model and in observations (at seasonal time scales, the correlation is ~0.26 for GOGA and ~0.42 for observations and LENS2). Despite this low correlation, the dominant ENSO signal in the large-scale atmospheric dynamics makes it difficult to ascertain the role of non-ENSO teleconnection patterns. To address this, we next analyze non-ENSO anomalies during wet and dry SWUS periods with similar background ENSO states.

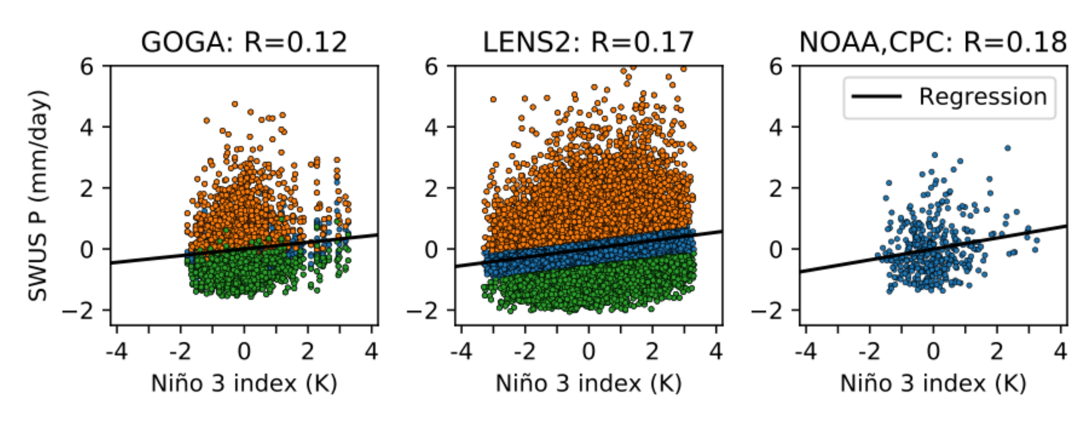

Fig. 3. Distribution of SWUS P anomalies as a function of the Niño 3 index for NDJFM months in GOGA (left), LENS2 (middle), and observations (right). The black line is the regression between SWUS P and Niño 3. Orange points indicate wet SWUS rain months used. Green points indicate dry SWUS rain months used.

b. Variability of the ENSO-SWUS precipitation teleconnection in LENS2 and GOGA

Focusing on non-ENSO teleconnections, we first calculate non-ENSO anomalies by regressing out the Niño 3 index as described in section 2c. Then, we create composites for NDJFM months with high non-ENSO SWUS rainfall minus low non-ENSO SWUS rainfall. In GOGA, which has ten ensemble members, we composite the three wettest minus the three driest ensemble members at each timestep. Note that in this case, each group has identical SST variability. In LENS2, which has a freely-evolving ocean, we take the wettest 30% minus the driest 30% of months over all the data. Using non-ENSO anomalies in conjunction with the composite method is effective at removing the ENSO signal from our analyses. We perform the analysis on NDJFM months rather than seasons, due to the larger sample size, although results are overall similar. Composite analyses are not performed on reanalysis data due to the small sample size.

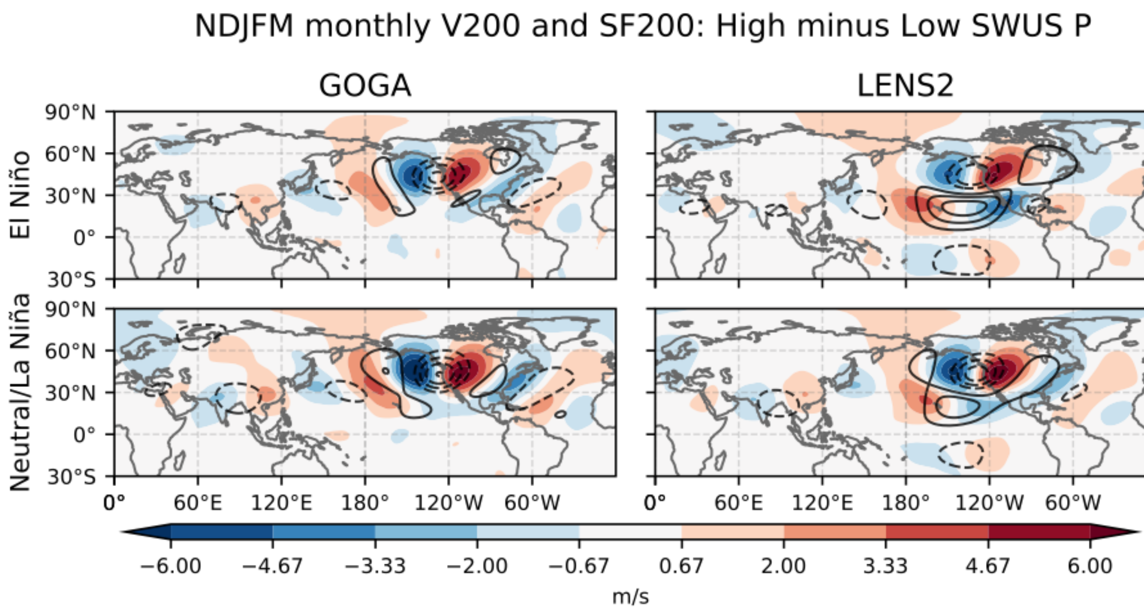

Fig. 4. Difference between high versus low SWUS rainfall months in GOGA (left column) and LENS2 (right column), and during positive ENSO (top row) and neutral/negative ENSO (bottom row). In each panel, 200 hPa meridional wind (shading) and 200 hPa streamfunction (contour) is plotted. The contour interval is $2.5 \cdot 10^6$ m^2 s^{-1}. The zero contour is omitted.

In anticipation that the ENSO background may affect which non-ENSO teleconnections drive SWUS precipitation variability, we compare El Niño periods where Niño 3 anomalies are greater than 0.5° C to neutral/La Niña periods where Niño 3 anomalies are less than 0.5° C. In addition, due to the wider distribution of Niño 3 anomalies in LENS2, only months with anomalies of magnitude 3.3° C and less are considered, in line with the historical record.

Figure 4 displays the composite results for 200 hPa meridional wind (V200) and SF200. There are two clear dominant patterns that are associated with non-ENSO SWUS precipitation. First, there is a zonal wavenumber-5 CGT with troughs over northern Africa, eastern India, the subtropical west Pacific, the ENP, and the Atlantic oceans. This pattern is the dominant pattern in GOGA during both ENSO states, as well as being present in LENS2 neutral/La Niña months. Comparatively, the pattern is weaker in LENS2 El Niño months. This result supports the previous findings of Teng and Branstator (2017) regarding the significant role CGT's may play in ENP ridges and troughs.

The second dominant pattern in Figure 4 is a meridional El Niño-like wavetrain in the central-eastern Pacific, with a ridge in the subtropical East Pacific and trough in the ENP. This pattern is most apparent in LENS2 El Niño months, which coincidentally had the weakest zonal pattern. The pattern is also apparent, albeit slightly weaker, in LENS2 neutral/La Niña months. In GOGA, the meridional wavetrain signal is much weaker if present at all.

Although the meridional wavetrain resembles an El Niño response, it is not a result of linear ENSO variability, due to the composite method and removal of linearly regressed ENSO anomalies. To affirm this and identify tropical forcing patterns for the circulation patterns in Figure 4, identically constructed composites for non-ENSO precipitation and non-ENSO SST are displayed in Figure 5. Analyzing SST first, there is no GOGA SST signal as expected. By contrast, LENS2 contains weak SST signals in the tropics and stronger SST signals in the extratropics, which are likely driven by the atmospheric circulation. All tropical SST differences are less than 0.25 K, so it appears that tropical SST variability is only weakly related to the differences in SWUS precipitation. However, it is possible that SST anomalies induced by the atmospheric variability may feedback on and modulate the atmospheric circulation in LENS2, even if they are not the direct drivers (e.g., Watanabe and Kimoto 2000, Lau and Nath 1996).

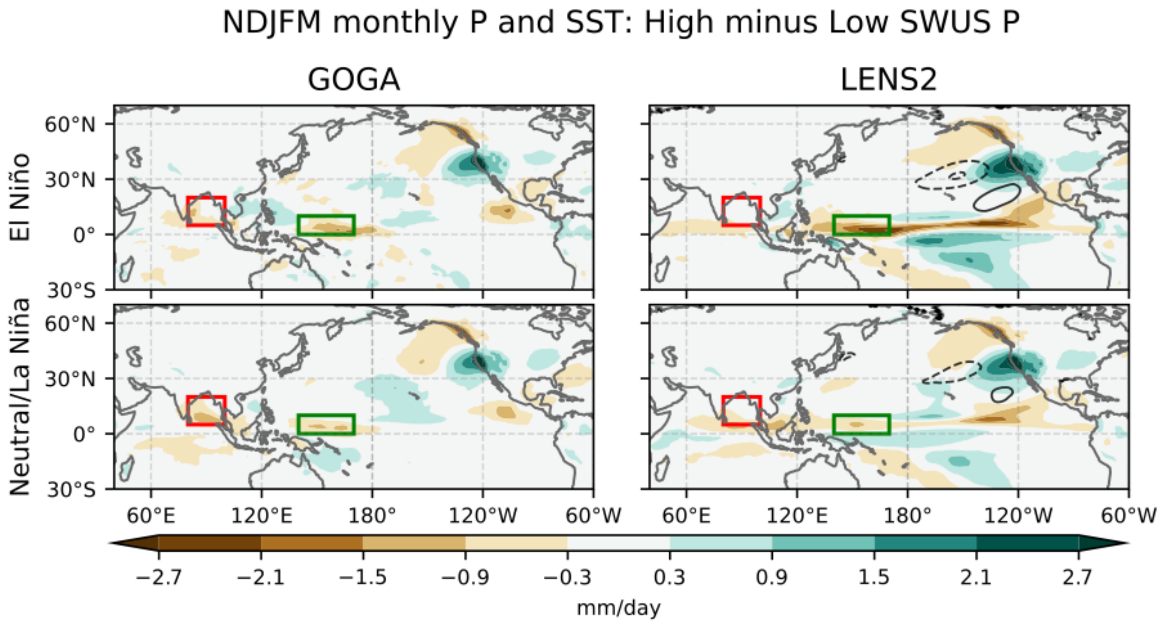

Fig. 5. As in Figure 4, but for precipitation (shading) and SST (contours). Contour interval is 0.25 K, with zero contour omitted. The red box is the NEIO (80°E-100°E, 5°N-20°N). The green box is the rainA region (140°E-170°E, 0°N-10°N).

Despite the lack of significant tropical SST differences, there are still significant tropical precipitation differences that appear unforced by SST and may explain the different circulation patterns present in each model experiment and ENSO state. First, in LENS2, there is a tropical Pacific precipitation pattern that resembles a southward shift and weakening of the Intertropical Convergence Zone (ITCZ). This pattern is stronger during LENS2 El Niño months relative to neutral/La Niña months, while not showing any significant presence in GOGA. The meridional wavetrain varied in a similar way with model experiment and ENSO state, so this tropical precipitation pattern may be associated with the meridional wavetrain pattern.

When we analyze precipitation in the West Pacific and Indian Ocean in Fig. 5, we note two significant features. First, there is a common signal in the rainA region (140°E-170°E, 0°N-10°N), highlighted by the green box, during each ENSO phase and each model experiment. Teng and Branstator (2017) found this precipitation signal to be associated with zonal wavetrain patterns that set up ridges or troughs in the ENP. Second, we highlight in red the region in the Northeast Indian Ocean (NEIO), which only contains a precipitation signal during GOGA neutral/La Niña months. Due to its proximity to the EAJS, we hypothesize that this precipitation signal may be related to the zonal wavetrain pattern. Later, in section 3e, we will analyze the atmospheric responses to precipitation in each of these regions to investigate why the rainA signal is common for each model experiment and ENSO phase, while the NEIO precipitation signal is strongest during GOGA neutral/La Niña months.

c. Clustering to identify unique teleconnections that bring SWUS precipitation

So far, we have visually identified two non-ENSO circulation patterns that can regulate SWUS precipitation: a zonal CGT and an East Pacific meridional wavetrain. However, it is possible that there are other unidentified patterns hidden within the composite, as it is difficult to disentangle individual circulation patterns. Additionally, the composite method offers no quantitative measure of the frequency of occurrence for individual patterns. To address this, we use a clustering algorithm to analyze wet SWUS months individually and to identify unique circulation patterns associated with SWUS precipitation. Then, we can assess the relative frequencies of the unique patterns, the tropical forcing associated with each pattern, and how the cluster frequencies change in each model set-up and with different ENSO backgrounds.

The method used for clustering anomalies is described in section 2d. Using non-ENSO SWUS precipitation, input months are selected as the wettest 30% of NDJFM months from the ten GOGA ensemble members and the wettest 30% of NDJFM months from the first ten ensemble members of LENS2, in order to equalize the influence from each one. Input variables include the first 20 EEOF's of non-ENSO V200 and non-ENSO SF200 over the ENP and North America (180°E-260°E, 20°N-70°N).

We find that searching for 3 clusters produces the best results, based on the BIC score and by visual inspection. Composites are constructed by assigning each month to one of the calculated clusters. The composites for precipitation and SF200 are displayed in Figure 6, along with the relative frequency of each cluster within each model experiment. Cluster frequencies and composites are also calculated for ERA5, although the results are less statistically reliable due to the smaller sample size. Additionally, we calculate the cluster frequencies for each ensemble member individually, then calculate the standard deviation of the ensemble spread.

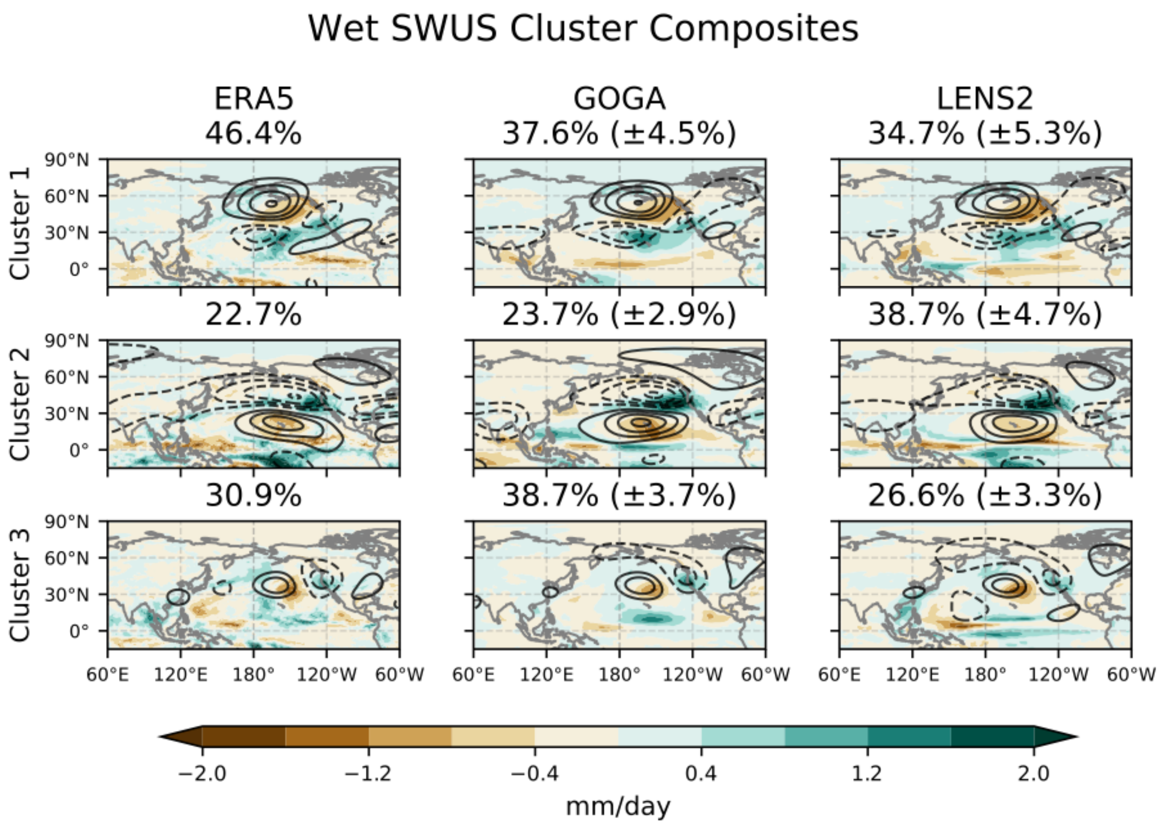

Fig. 6. Composite non-ENSO anomalies for each cluster in ERA5, GOGA, and LENS2. Monthly NDJFM SF200 (contours) and precipitation (shading). Contour interval is $2.5 \cdot 10^6\ m^2/s$. Zero contour is omitted. Frequency of each cluster in each dataset is displayed in subplot title, with ensemble member standard deviation in parentheses.

Cluster 1 (top row) can be described as an arching wavetrain that strongly resembles the PNA teleconnection pattern and is similar to patterns found previously associated with non-ENSO precipitation in the SWUS (e.g., Li et al 2019, Lopez and Kirtman 2019, Jiang et al. 2022). The cluster is associated with different tropical precipitation patterns in each dataset. In ERA5, there are only very weak tropical anomalies. By contrast, the arching wavetrain is associated with precipitation in the West Pacific rainA region in GOGA. In LENS2, it is associated with a quadrupole of precipitation anomalies over the equatorial and off-equatorial Pacific. These differences highlight a potentially strong role for internal atmospheric variability for Cluster 1. Despite this, Cluster 1 is the most common cluster in ERA5 and GOGA, and second most common in LENS2, despite not being one of the wavetrains identified earlier in our composite analysis.

Cluster 2 (middle row) is associated with a meridional wavetrain, shifted slightly westward relative to the meridional wavetrain found earlier (Figure 4 right column), so that it resembles more closely the regressed ENSO response (Figure 1). This pattern, compared to the other clusters, is associated with stronger precipitation anomalies in the tropical Pacific. In particular, in each model experiment this cluster is associated with a north-south dipole of precipitation in the central tropical Pacific, as well as a north-south dipole of opposite sign in the tropical West Pacific. This cluster is nearly twice as common in LENS2 (38.7%) as it is in ERA5 (22.7%) and GOGA (23.7%).

Lastly, Cluster 3 is a zonal wavetrain that resembles the composite atmospheric pattern associated with SWUS precipitation in GOGA (Figure 4 left column). It is a zonal wavenumber 5 wavetrain that propagates through the EAJS and sets up a trough over the ENP region. It is associated with excess precipitation in Southeast China and the off-equatorial central North Pacific in each dataset, although this signal is weaker in GOGA relative to ERA5 and LENS2. This cluster is more frequent in GOGA (38.7%) than it is in LENS2 (26.6%) and ERA5 (30.9%).

In addition to variations with model, cluster frequencies may also depend on the ENSO background state, which may modulate non-ENSO variability (e.g., by changing preferential non-ENSO convection patterns in the tropics, propagation of Rossby waves in the extratropics, etc.). Figure 7 displays the frequency for each cluster during El Niño and neutral/La Niña backgrounds for each experiment. For all datasets, the zonal and arching wavetrain clusters are more prevalent during neutral/La Niña backgrounds than during El

Niño, while the meridional wavetrain cluster is more prevalent during El Niño backgrounds. The fact that each of ERA5, GOGA, and LENS2 displays similar cluster relationships with ENSO phase, despite their differences, indicates the robustness of this dependence on ENSO.

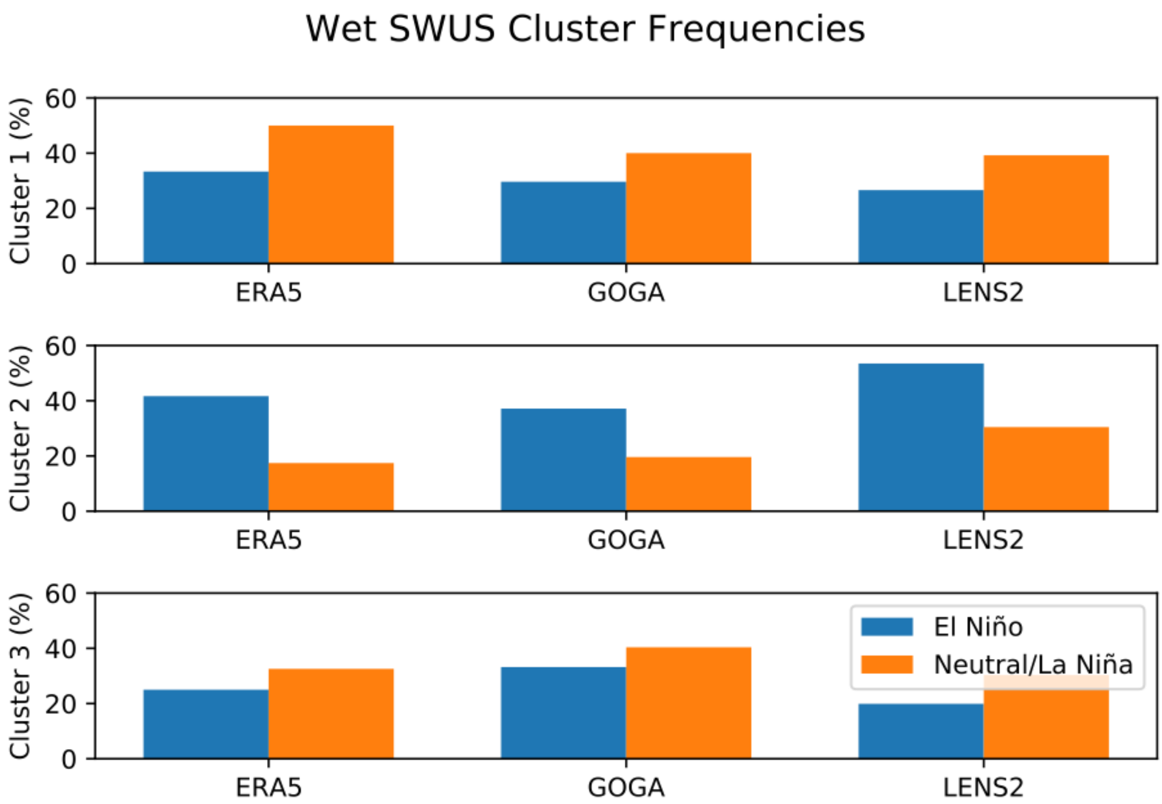

Fig. 7. Cluster frequencies for each cluster in Figure 6 for each dataset and ENSO phase.

d. Role of the background flow on Rossby waveguide characteristics

So far, we have identified three clusters associated with non-ENSO SWUS rainfall and found that both model choice and the ENSO background state influence cluster frequency. There are many potential causes for these differences, such as differences in tropical convective variability (e.g., MJO, ITCZ), modulations of Rossby wave source and propagation by the atmospheric mean state, and different internal midlatitude atmospheric dynamics. All of these likely play a role in modulating cluster frequencies, and each may be affected by model setup and ENSO phase. However, for the rest of this paper, we will focus on the waveguide effect of the atmospheric mean state, with a brief discussion of the differences in tropical convective variance and Rossby wave source in Section 3f. We now turn to how changes in the background flow due to model biases and ENSO can affect the characteristics of the waveguide in the North Pacific, with potentially significant effects on Rossby wavetrains that impact SWUS precipitation.

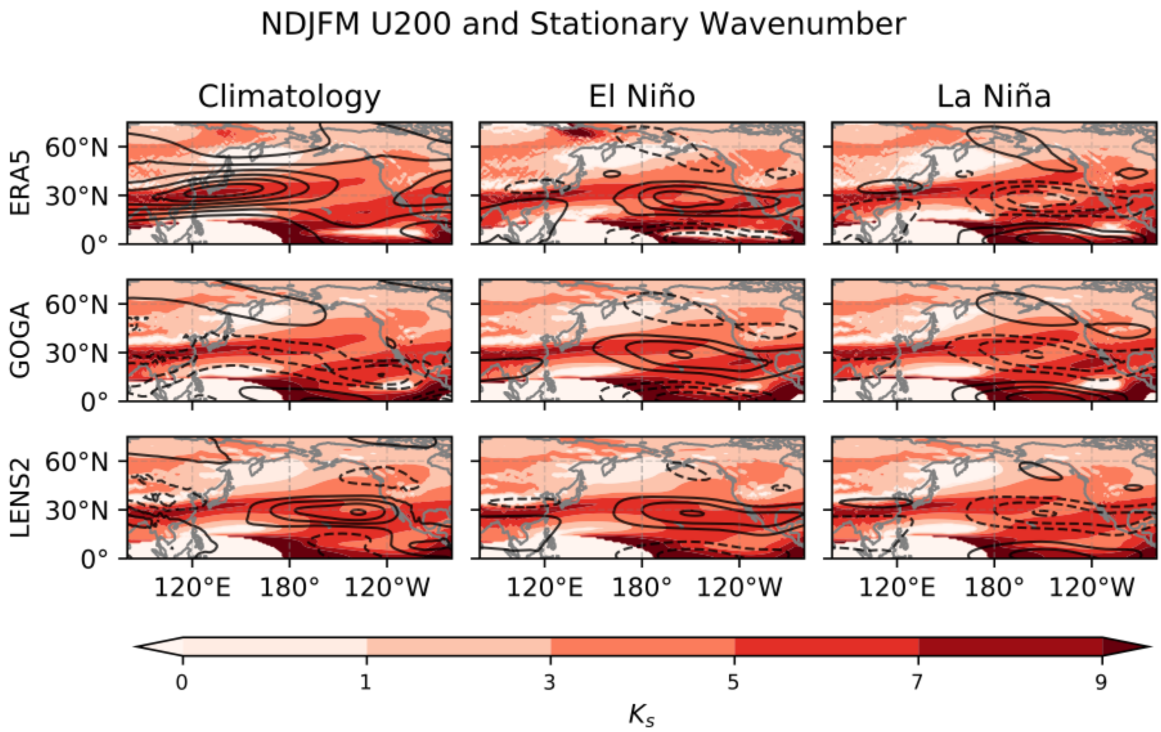

Fig. 8. (left) NDJFM climatological U200 for ERA5 (top) and corresponding biases in GOGA (middle) and LENS2 (bottom), as well as NDJFM climatological stationary wavenumber in ERA5, GOGA, and LENS2. (middle) NDJFM U200 regressed response to El Niño and corresponding stationary wavenumber for ERA5, GOGA, and LENS2. (right) As in middle column but for La Niña. Contour intervals are 10 m/s (top left) and 2.5 m/s (elsewhere). In each panel, U200 is contoured, and stationary wavenumber is shaded.

To investigate the role of the basic state on Rossby wave propagation, we calculate the ERA5 NDJFM climatological U200 and the mean U200 biases in GOGA and LENS2, respectively (Figure 8 left column). We also calculate the climatological NDJFM stationary wavenumber for each experiment (section 2e).

In ERA5, the climatological jet stream over Southeast Asia forms a narrow strip of maximum K_s that serves as an effective waveguide through the EAJS. This waveguide extends toward the Eastern North Pacific, while a separate waveguide forms in the tropical/subtropical Eastern Pacific that is later associated with the Atlantic jet stream.

In the model experiments, LENS2 displays stronger zonal wind biases in the North Pacific that have more significant effects on the stationary wavenumber field, compared to GOGA. While GOGA is characterized by a similar North Pacific waveguide as in reanalysis, LENS2 displays a nearly 10 m/s strengthening of the subtropical eastern Pacific westerlies, which is associated with a strong increase in the meridional vorticity gradient in the central and eastern subtropical Pacific, with a smaller decrease on the poleward side of the jet. This is associated with a southward shift in the waveguide, with a westward retraction in the midlatitude ENP region and eastward extension in the subtropics.

This change in the waveguide can have significant effects on Rossby wave propagation, particularly for high wavenumber (short length) waves. Considering regions with $K_s \geq 5$, where CGT's of zonal wavenumber 5 are theoretically bound, both ERA5 and GOGA are characterized by a North Pacific waveguide that extends towards the ENP, so that wavenumber 5 wavetrains from the EAJS propagate zonally into the ENP. In LENS2, changes in the East Pacific waveguide cause the same waves to deviate southward to join the southern waveguide, at least according to linear theory and on a climatological basis.

Similarly, differences in the background flow due to ENSO may alter the stationary wavenumber field and Rossby wave propagation. Figure 8 displays the regressed U200 anomalies associated with El Niño (middle column) and La Niña (right column), as well as the average stationary wavenumber field that occurs during each ENSO phase. Notably, the ENSO driven jet response is similar to the mean bias in LENS2, and it has similar effects on the waveguide. During El Niño, there is a westward retraction of the midlatitude waveguide in the North Pacific, while in La Niña there is greater eastward extension into the midlatitude ENP region. Curiously, La Niña can be thought to counteract the LENS2 mean state bias, such that during LENS2 La Niña, the waveguide is similar to that which occurs during ERA5 and GOGA El Niño.

The dependence of the waveguide on model mean state biases and ENSO phase may partially explain some of the cluster frequency dependences found earlier, particularly for the zonal wavetrain pattern, which has a higher zonal wavenumber. For example, during La Niña, EAJS zonal wavetrains may propagate into the ENP more frequently, due to the eastward, northward extension of the waveguide relative to El Niño. Through identical reasoning, GOGA may be dominated by the zonal wavetrain variability more than LENS2. In this way, it appears that large-scale changes in the background flow, due to ENSO, model biases, or other variabilities, may result in significant changes to the waveguide, Rossby wave propagation, and potentially teleconnection sign and strength.

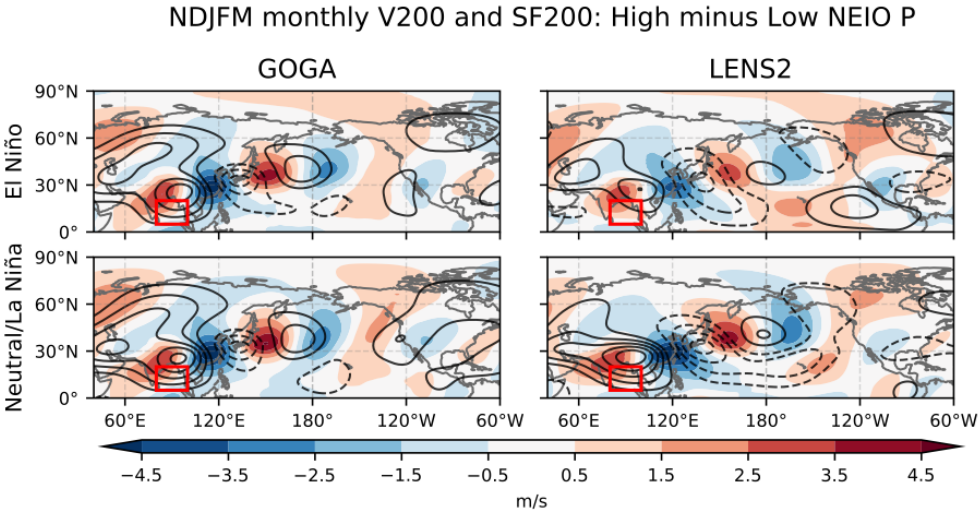

Fig. 9. Difference between high versus low Northeast Indian Ocean rainfall months in GOGA (left column) and LENS2 (right column), as well as in positive ENSO (top row) and neutral/negative ENSO (bottom row). 200 hPa meridional wind (shading) and 200 hPa streamfunction (contour) is plotted. The contour interval is $1.5 \cdot 10^6$ m^2 s^{-1}, with zero contour omitted. NEIO precipitation region is indicated by red box.

e. Effect of the background state on SWUS precipitation teleconnections

Although we have demonstrated how changes in the background flow can affect the waveguide, it is still necessary to confirm its effects on Rossby wave propagation and SWUS precipitation. We now construct composites on rainfall in the NEIO (red box from Figure 5) and in the rainA region (green box from Figure 5), to demonstrate how the waveguide affects two types of Rossby wavetrains. Composites are calculated in an identical manner to Figures 4 and 5, but replacing SWUS precipitation with the NEIO or rainA precipitation, in order to analyze the non-ENSO response to NEIO and rainA precipitation.

In Figure 9, the atmospheric circulation associated with NEIO precipitation consists of a zonally oriented wavetrain in the EAJS, which is similar in each model experiment and ENSO phase. However, significant differences emerge as the wavetrain propagates downstream towards the East Pacific.

During GOGA El Niño months, the wavetrain deviates southward in the East Pacific before continuing zonally eastward. Contrarily, in GOGA neutral/La Niña months, the wavetrain continues to propagate zonally eastward through the midlatitudes over the ENP and the United States. This aligns with the subtropical bias of the East Pacific waveguide during El Niño, relative to La Niña. Due to the meridional shift of the wavetrain, NEIO precipitation is associated with a neutral SWUS rain response in GOGA El Niño months and a dry SWUS in GOGA neutral/La Niña months (Figure 10).

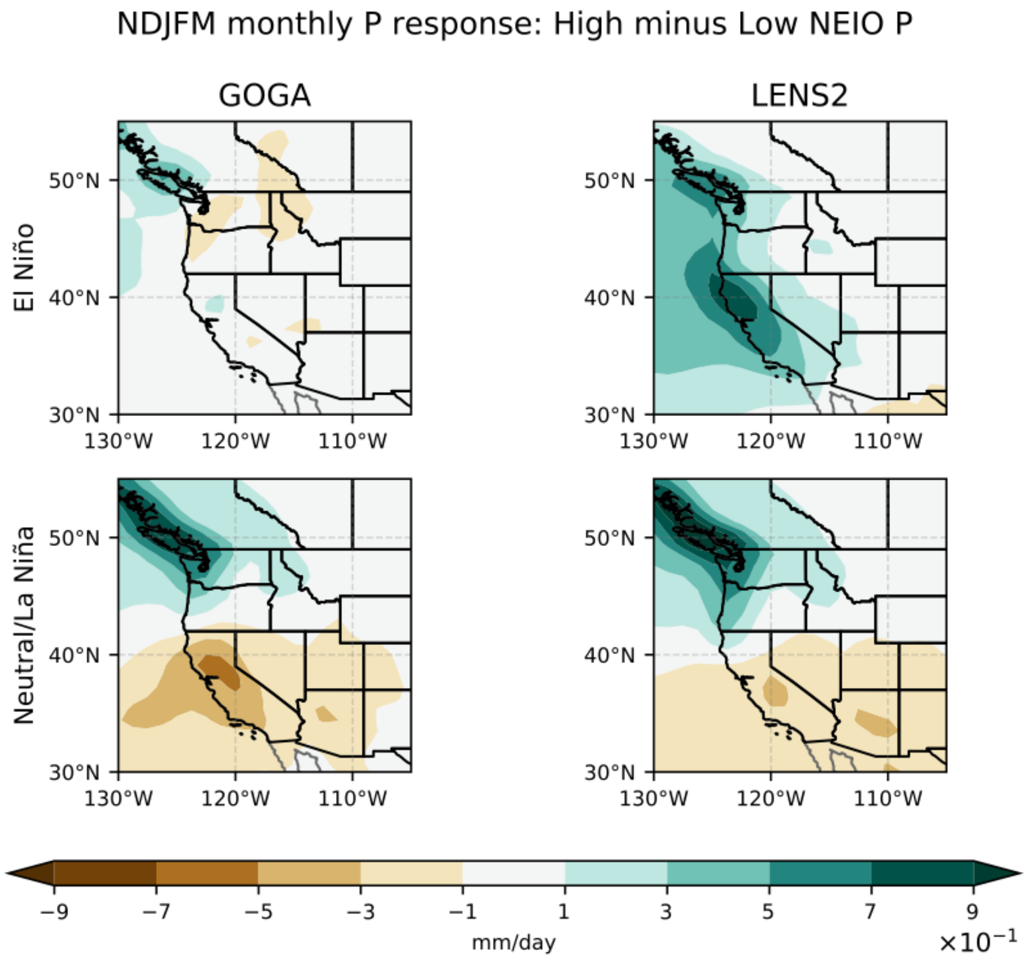

Fig. 10. Difference between high versus Northeast Indian Ocean rainfall months in GOGA (left column) and LENS2 (right column), as well as in positive ENSO months (top row) and neutral/negative ENSO (bottom row). In each panel, Western North America precipitation (shading) is plotted.

Analyzing LENS2, there is a notable similarity between the circulation pattern during LENS2 neutral/La Niña months and GOGA El Niño months. However, this is not surprising considering that the waveguide and stationary wavenumber field during LENS2 La Niña was similar to that during GOGA El Niño. Slight differences do lead to a slightly drier SWUS in LENS2 neutral/La Niña months.

During LENS2 El Niño months, there appears to be even further southward deviation of the EAJS wavetrain once it approaches the East Pacific, so that the weak trough over Alaska in LENS2 neutral/La Niña months has shifted southward into the ENP. However, it is important to note that NEIO precipitation during LENS2 El Niño is associated with relatively higher precipitation variability in the central tropical Pacific, relative to La Niña and GOGA, which may obfuscate the response. In any case, NEIO precipitation is associated with a wet SWUS during El Niño in LENS2, contrasting the drier response during neutral/La Niña months.

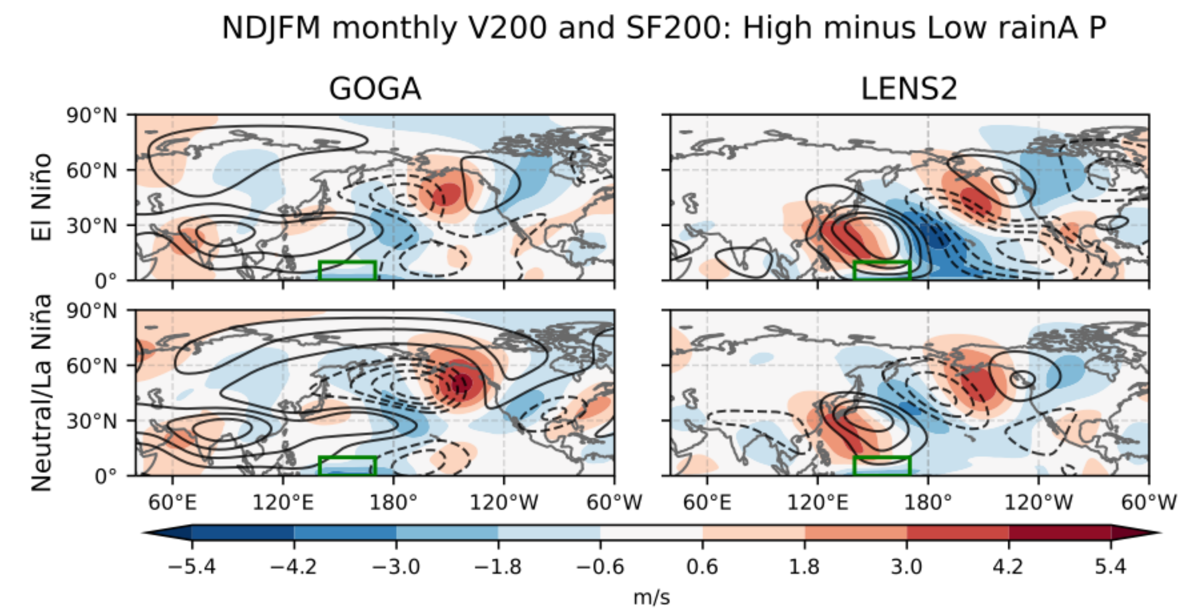

Fig. 11. Difference between high versus low rainA rainfall months in GOGA (left column) and LENS2 (right column), as well as in positive ENSO (top row) and neutral/negative ENSO (bottom row). 200 hPa meridional wind (shading) and 200 hPa streamfunction (contour) is plotted. The contour interval is $1.5 \cdot 10^{6}\ \mathrm{m}^{2}\ \mathrm{s}^{-1}$. The zero contour is omitted. rainA precipitation region is indicated by green box.

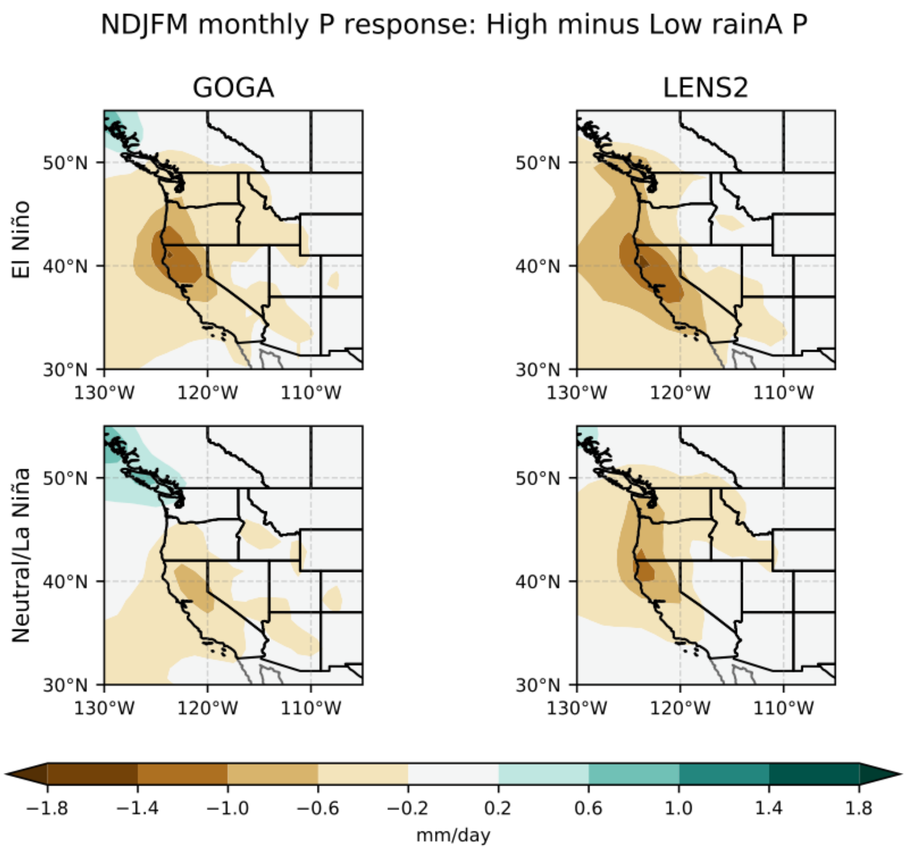

Fig. 12. Difference between high versus low rainA rainfall months in GOGA (left column) and LENS2 (right column), as well as in positive ENSO months (top row) and neutral/negative ENSO (bottom row). In each panel, Western North America precipitation (shading) is plotted.

Lastly, we have analyzed the response to precipitation in the rainA region (Figure 11). It is associated with an arching wavetrain response that resembles the PNA, and thus may be related to Cluster 1. Comparing El Niño to neutral/La Niña in GOGA, there does seem to be a slight southward shift during El Niño, but it is not significantly enough to change the dry SWUS response (Figure 12). In LENS2, there are more impacts from covarying tropical precipitation patterns in the central Pacific, but the wavetrains are largely similar and set up a ridge in the ENP, associated with dry anomalies in the SWUS. Thus, differences in the waveguide due to model bias and ENSO did not significantly alter Rossby wave propagation enough to alter SWUS rain anomalies. In this way, it is likely that the role of the waveguide is more important for short wavelength zonal wavetrains than long wavelength arching wavetrains. This may potentially explain why the zonal wavetrain cluster frequency differs between GOGA and LENS2, while the arching wavetrain cluster frequency is comparable for both.

3f. Potential role of tropical forcing and Rossby wave source

While we have shown how biases in the waveguide can modulate zonal wavetrains and likely affect the frequency of the Cluster 3 zonal wavetrain pattern, we still do not have an adequate explanation for the increased frequency in LENS2 (38.7%) for the Cluster 2 meridional wavetrain, relative to GOGA (23.7%) and ERA5 (22.7%). Due to the strong tropical precipitation signal associated with SWUS precipitation in the LENS2 composites (Figure 5) and in Cluster 2 (Figure 6), the frequency difference is likely related to tropical forcing. In particular, we are interested in two possible mechanisms related to tropical forcing. First, there is the amount of tropical convective activity (represented by standard deviation), where we expect that if LENS2 has increased convective activity in the tropics, there might be increased activity in the meridional Cluster 2 pattern. Second, the LENS2 subtropical Pacific jet bias, which increases the meridional vorticity gradient in the vicinity of the strengthening, may increase the sensitivity of Rossby wave source to meridional divergent outflow (Sardeshmukh and Hoskins 1988). In this section, we briefly analyze and link these two possibilities to the meridional wavetrain pattern by comparing the tropical upper level divergence activity between each of LENS2, GOGA, and ERA5, and analyzing the extratropical response to a region of increased tropical divergence activity in LENS2.

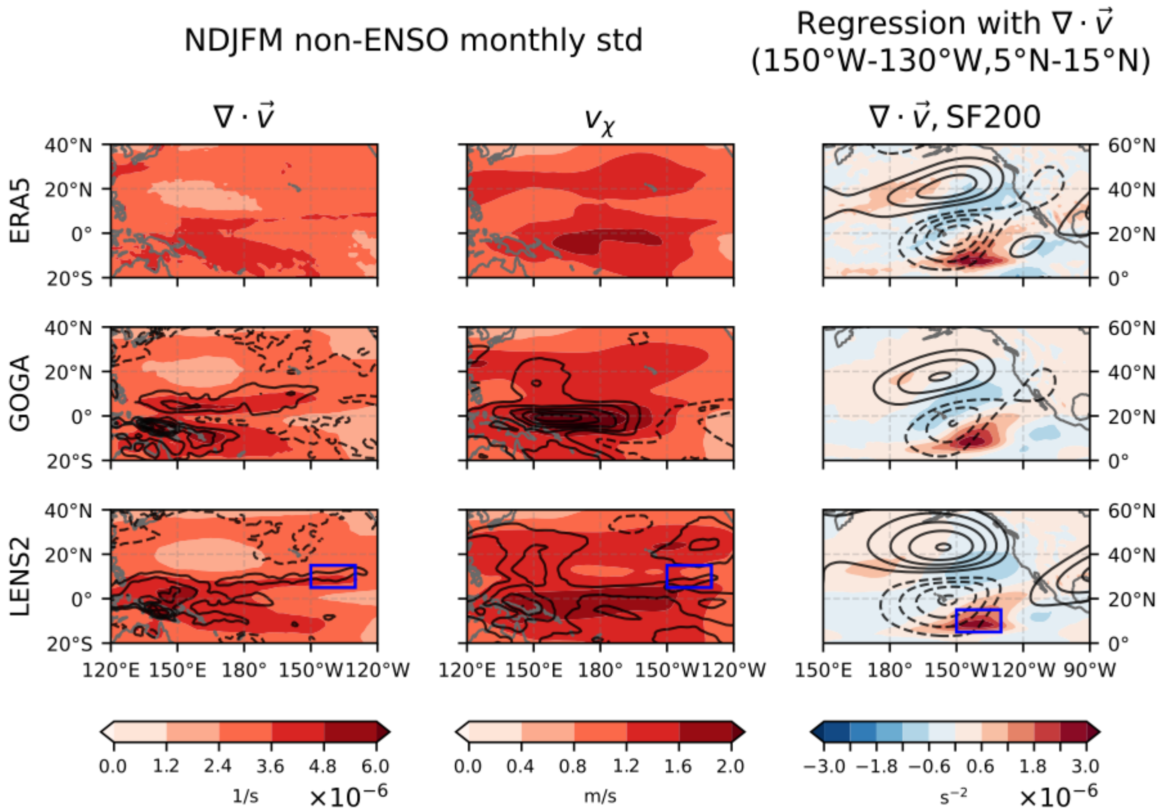

Fig. 13: (left) non-ENSO NDJFM standard deviation of monthly 200 hPa divergence (shading) and bias from ERA5 (contour). (middle) as in left column but for the irrotational meridional wind. Contour intervals are $0.5 \cdot 10^{-6}\ s^{-1}$ (left) and $0.15\ m/s$ (middle), with zero contour omitted. (right) Normalized regression response to divergence in blue box (150°W-130°W,5°N-15°N) for 200 hPa divergence (shading) and streamfunction (contour). Contour interval is $1 \cdot 10^{6}\ m^{2}\ s^{-1}$, with zero contour omitted.

Analyzing the standard deviation of tropical divergence (Figure 13 left), most of the variance is associated with the north Pacific ITCZ and the South Pacific Convergence Zone (SPCZ) in each of the datasets. However, both LENS2 and GOGA exhibit increased activity over the Western Pacific and the ITCZ, relative to ERA5. The regions of increased divergence activity are associated with regions of increased meridional divergent flow activity (Figure 13 middle). In GOGA, this increased activity occurs in the equatorial central-western Pacific, between the SPCZ and the ITCZ. In LENS2, there is increased meridional divergent flow activity in the Eastern and Western Pacific, in particular. We expect that regions of increased meridional wind activity are also associated with increased variance in Rossby wave source from the advection of the mean state vorticity and potentially Rossby waves propagating to the extratropics.

To relate the tropical divergence activity differences to the meridional wavetrain frequency, we now choose a region at the eastern tip of the ITCZ where LENS2 exhibits increased activity relative to both GOGA and ERA5 (blue box, 150°W-130°W,5°N-15°N), which is associated with lobes of increased meridional divergent flow activity to the north and south. We calculate the non-ENSO regression response to the areal mean of divergence in this region (Figure 13 right), normalized by the standard deviation in LENS2 ($1.85 \cdot 10^{-6}\ \mathrm{s}^{-1}$), which was nearly 20% higher than the standard deviation in GOGA ($1.60 \cdot 10^{-6}\ \mathrm{s}^{-1}$) and in ERA5 ($1.56 \cdot 10^{-6}\ \mathrm{s}^{-1}$). Positive (negative) divergence is associated with a meridional wavetrain that weakens (strengthens) the subtropical jet and induces a dry (wet) response in the SWUS. Thus, there appears to be a clear link between the overestimation of tropical convective activity and the higher frequency of the meridional Cluster 2 wavetrain pattern in LENS2.

It is less clear, however, whether the subtropical jet bias affects the wavetrain response to the tropical divergence. Based on previous studies (e.g., Wang et al. 2020, Garfinkel and Hartmann 2010), we would have expected an equal tropical divergence to produce a stronger wavetrain amplitude in LENS2 due to the increased meridional vorticity gradient. However, while there is a change in orientation of the wavetrain in ERA5 and GOGA compared to LENS2, the amplitude of the response is similar in ERA5 while much weaker in GOGA. It is possible that other factors are affecting the extratropical response, such as air-sea feedbacks in the extratropics or the specific shape of the tropical convective pattern, which complicates the situation. Idealized modeling studies that prescribe a basic state wind and tropical heating would likely be required to separate and diagnose the effect of the jet bias from other variabilities.

3g. Implications for future climate change

While the focus of this study is on analyzing model variability, it is interesting to examine how regional climate variability may change in the future due to global warming. As such, we now briefly compare the LENS2 historical period (1948-2020) with the simulation of the last 3 decades of the 21st century in LENS2 (2071-2100), based on the SSP3 RCP 7.0 scenario.

Figure 14 displays the future change in the basic state zonal wind, as well as the future change in the tropical divergence activity. Similar to previous multi-model studies, there is an extension of the subtropical jet in the Pacific in future simulations under LENS2 (Allen and Luptowitz 2017, Wang et al. 2022). This strengthening in the subtropics increases the meridional vorticity gradient and results in a strengthened southward shift of the waveguide (i.e., in the direction of the LENS2 model bias). Previous studies have shown that such future changes in the basic state may result in eastward shifted teleconnection patterns (Zhou et al. 2020, Wang et al. 2022). In addition, there may be similar effects as previously discussed for zonal wavetrains and Rossby wave source. Besides the basic state wind, there is an increase in divergent wind activity in the equatorial East Pacific, in line with previous studies that have found increased MJO precipitation activity in the East Pacific (e.g., Wang et al. 2022, Maloney et al. 2019), and a decrease in West Pacific divergent wind activity.

These changes are likely associated with the El Niño-like warming of the tropical East Pacific in future LENS2 (not pictured), and they may alter the frequencies of teleconnection patterns affecting SWUS precipitation. In fact, we find that when calculating cluster frequencies in future LENS2 simulations using the historical cluster patterns, there is a decrease in the arching Cluster 1 (34.7% → 29.9%), an increase in the meridional Cluster 2 (38.7% → 45.2%) and a slight decrease in zonal Cluster 3 (26.6% → 24.9%). The decrease in Cluster 1 and increase in Cluster 2 is in agreement with the increase in East Pacific divergent flow activity and decrease in West Pacific divergent flow activity. It is consistent with the mechanisms we describe in section 3f and also consistent with the previously found relationship between ENSO and cluster frequency (Figure 7), suggesting that projected El Niño-like climate change reinforces the existing model biases in LENS2. This illustrates how model bias may affect future projections of SWUS precipitation, a region where climate projections are notoriously uncertain (e.g., Gershunov et al. 2019).

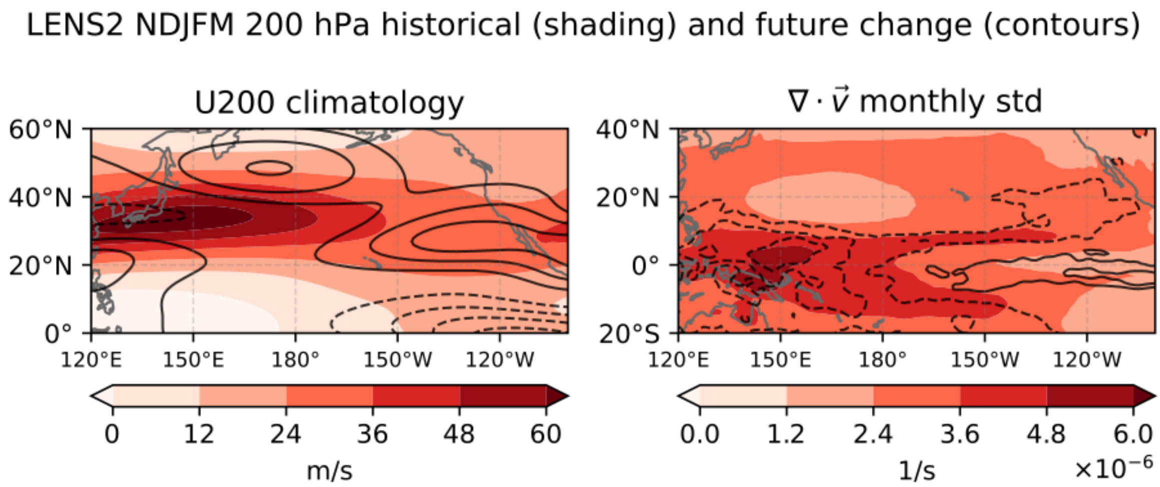

Fig. 14: (left) LENS2 historical NDJFM U200 climatology (shading) and change in LENS2 future SSP370 scenario (contour). Contour level is 2 m/s, with zero contour omitted. (right) non-ENSO NDJFM standard deviation of monthly 200 hPa divergence in LENS2 historical (shading) and change in LENS2 future SSP370 scenario (contour). Contour interval is $0.3 \cdot 10^{-6}\ s^{-1}$, with zero contour omitted.

4. Summary and Conclusions

In this study, we have analyzed monthly wintertime SWUS precipitation variability in reanalysis and in both a coupled (LENS2) and atmosphere-only model setup (GOGA). The objective of the study was threefold: 1) extract the dominant non-ENSO teleconnection patterns that influence SWUS precipitation during the cool season (NDJFM), 2) reveal the influence of the background state on the non-ENSO teleconnections and 3) compare the frequency and fidelity of these teleconnection patterns in LENS2 and GOGA.

Composite analyses suggest that non-ENSO SWUS precipitation in GOGA is strongly associated with zonal wavetrains, while in LENS2 meridional wavetrains have a stronger influence. The meridional wavetrain is associated with precipitation in the tropical central and eastern Pacific that resembles a southward shift or weakening of the ITCZ. Meanwhile, the zonal wavetrain is potentially associated with Indian Ocean and West Pacific precipitation, similar to findings from Teng and Branstator (2017). A clustering algorithm that extracts non-ENSO patterns associated with wet SWUS winter months also supports and refines these results. The algorithm identifies three major clusters: an arching wavetrain that resembles the PNA, a meridional "ENSO-like" wavetrain over the central North Pacific, and a zonal CGT-type wavetrain pattern. The zonal wavetrain pattern most often occurs in GOGA, while the meridional wavetrain pattern occurs most commonly in LENS2. The meridional wavetrain cluster displayed strong associations with tropical Pacific precipitation, in contrast to the PNA-type cluster, which displayed only weak tropical precipitation anomalies, in agreement with previous studies separating the influence of the PNA and ENSO-type teleconnections (Li et al. 2019, Lopez and Kirtman 2019).

Since LENS2 and GOGA use the same atmospheric model (CAM6), these differences cannot be attributed to differences in atmospheric model physics or parameterizations. However, differences in their ocean representations do lead to differences in the atmospheric mean state. In GOGA, the background flow over the North Pacific is similar to the ERA5 reanalysis, with an EAJS waveguide that extends northward and eastward across the Pacific into the ENP. In contrast, LENS2 has a westerly bias in the eastern Pacific subtropical westerlies, which leads to a westward retraction of the midlatitude waveguide and extension of the subtropical waveguide associated with the southward shift of the meridional vorticity gradient. The LENS2 bias is similar to an El Niño forced response, which is associated with a westward retracted (eastward extended) East Pacific midlatitude waveguide during El Niño (La Niña).

The differences in background flow, and thus the waveguide, alter how remote forcing affects SWUS precipitation. For example, NEIO precipitation excites a zonally oriented wavetrain (wavenumber 5) in the EAJS in both ensembles, but the wave propagates differently in the East Pacific depending on the waveguide characteristics in GOGA versus LENS2. This is also true for differences between each ENSO phase, and it results in differing patterns on SWUS precipitation in response to the NEIO remote forcing. The influence of the waveguide is not as pronounced for larger scale arching wavetrains. For example, the arching wavetrain in response to tropical West Pacific precipitation is similar in GOGA and LENS2 and for each ENSO phase, resulting in similar rain responses in the SWUS.

In summary, variations in atmospheric basic state due to different SST variability, while using the same atmospheric model, may significantly affect teleconnections that regulate SWUS precipitation and their frequency, although there are other factors that also likely play an important role such as the variance of tropical convective activity and the modulation of Rossby wave source by the mean state vorticity gradient. As shown by previous studies (e.g., Henderson et al. 2017), models must accurately model both tropical convective variability and the atmospheric mean state, or else forecast accuracy of remote extratropical regions will likely be limited. Even in the field of S2S and seasonal prediction, where models are initialized from observational data and only run for a short period of time, persistent model biases quickly emerge that may affect forecast fidelity (Garfinkel et al. 2022), and understanding these biases in the S2S/seasonal prediction models is critical to achieve higher skill in S2S prediction of SWUS P.

Understanding these biases will likely require a combination of analysis of model output from operational forecast models, such as from the S2S and NMME (Kirtman et al. 2014) databases, and idealized modeling studies which can prescribe tropical heating and basic states (e.g., Watanabe and Kimoto 2000, Wang et al 2020, Henderson et al. 2017). There is a continued need to refine our understanding of systematic biases in long-range prediction models to inform potential avenues for model improvement and higher prediction skill.

Acknowledgments.

We gratefully acknowledge the support by the California Department of Water Resources (Contract 4600013127). We are also grateful to three reviewers whose comments improved the manuscript.

Data Availability Statement.

ERA5 data was provided by the Copernicus Climate Change Service at https://cds.climate.copernicus.eu/ (C3S 2023). CPC precipitation data and NOAA ERSSTv5 data provided by the NOAA PSL, Boulder, Colorado, USA, from their website at https://psl.noaa.gov. LENS2 and GOGA ensemble data provided by NCAR from their website at https://www.cesm.ucar.edu/.

REFERENCES

Allen, R.J. and Luptowitz, R., 2017. El Niño-like teleconnection increases California precipitation in response to warming. *Nature communications*, *8*(1), 16055. https://doi.org/10.1038/ncomms16055

Arcodia, M.C., Kirtman, B.P. and Siqueira, L.S., 2020. How MJO teleconnections and ENSO interference impacts US precipitation. *J. Climate*, *33*(11), 4621-4640. https://doi.org/10.1175/JCLI-D-19-0448.1

Becker, E.J., Kirtman, B.P., L'Heureux, M., Muñoz, Á.G. and Pegion, K., 2022. A decade of the North Amer. Multimodel Ensemble (NMME): Research, application, and future directions. *Bull. Amer. Meteor. Soc.*, *103*(3), E973-E995. https://doi.org/10.1175/BAMS-D-20-0327.1

Branstator, G., 2002. Circumglobal teleconnections, the jet stream waveguide, and the North Atlantic Oscillation. *J. Climate*, *15*(14), 1893-1910. https://doi.org/10.1175/1520-0442(2002)015<1893:CTTJSW>2.0.CO;2

Branstator, G. and Teng, H., 2017. Tropospheric waveguide teleconnections and their seasonality. *J. Atmos. Sci.*, *74*(5), 1513-1532. https://doi.org/10.1175/JAS-D-16-0305.1

Capotondi, A., Deser, C., Phillips, A.S., Okumura, Y. and Larson, S.M., 2020. ENSO and Pacific decadal variability in the Community Earth System Model version 2. *Journal of Advances in Modeling Earth Systems*, *12*(12), p.e2019MS002022. https://doi.org/10.1029/2019MS002022

Cohen, J., Pfeiffer, K. and Francis, J., 2017. Winter 2015/16: A turning point in ENSO-based seasonal forecasts. *Oceanography*, *30*(1), 82-89.

Copernicus Climate Change Service, Climate Data Store 2023: ERA5 monthly averaged data on pressure levels from 1940 to present. Copernicus Climate Change Service (C3S) Climate Data Store (CDS), https://doi.org/10.24381/cds.6860a573

Danabasoglu, G., Lamarque, J.F., Bacmeister, J., Bailey, D.A., DuVivier, A.K., Edwards, J., Emmons, L.K., Fasullo, J., Garcia, R., Gettelman, A. and Hannay, C., 2020. The community earth system model version 2 (CESM2). *Journal of Advances in Modeling Earth Systems*, *12*(2), p.e2019MS001916. https://doi.org/10.1029/2019MS001916

DeFlorio, M.J., Waliser, D.E., Ralph, F.M., Guan, B., Goodman, A., Gibson, P.B., Asharaf, S., Monache, L.D., Zhang, Z., Subramanian, A.C. and Vitart, F., 2019. Experimental subseasonal-to-seasonal (S2S) forecasting of atmospheric rivers over the Western United States. *J. Geophys. Res.: Atmos.*, *124*(21), 11242-11265. https://doi.org/10.1029/2019JD031200

DeMott, C.A., Klingaman, N.P., Tseng, W.L., Burt, M.A., Gao, Y. and Randall, D.A., 2019. The convection connection: How ocean feedbacks affect tropical mean moisture and MJO propagation. *J. Geophys. Res.: Atmos.*, *124*(22), 11910-11931. https://doi.org/10.1029/2019JD031015

Deser, C., Simpson, I.R., Phillips, A.S. and McKinnon, K.A., 2018. How well do we know ENSO's climate impacts over North America, and how do we evaluate models accordingly?. *J. Climate*, *31*(13), 4991-5014. https://doi.org/10.1175/JCLI-D-17-0783.1

Dettinger, M.D., 2013. Atmospheric rivers as drought busters on the US West Coast. *J. Hydrometeor.*, *14*(6), 1721-1732. https://doi.org/10.1175/JHM-D-13-02.1

Garfinkel, C.I. and Hartmann, D.L., 2010. Influence of the quasi-biennial oscillation on the North Pacific and El Niño teleconnections. *J. Geophys. Res.: Atmos.*, *115*(D20). https://doi.org/10.1029/2010JD014181

Garfinkel, C.I., Weinberger, I., White, I.P., Oman, L.D., Aquila, V. and Lim, Y.K., 2019. The salience of nonlinearities in the boreal winter response to ENSO: North Pacific and North America. *Climate Dynamics*, *52*, 4429-4446. https://doi.org/10.1007/s00382-018-4386-x

Garfinkel, C.I., Chen, W., Li, Y., Schwartz, C., Yadav, P. and Domeisen, D., 2022. The winter North Pacific teleconnection in response to ENSO and the MJO in operational subseasonal forecasting models is too weak. *J. Climate*, *35*(24), 4413-4430. https://doi.org/10.1175/JCLI-D-22-0179.1

Gershunov, A., Shulgina, T., Clemesha, R.E., Guirguis, K., Pierce, D.W., Dettinger, M.D., Lavers, D.A., Cayan, D.R., Polade, S.D., Kalansky, J. and Ralph, F.M., 2019. Precipitation regime change in Western North America: the role of atmospheric rivers. *Scientific reports*, *9*(1), 9944.

Gibson, P.B., Waliser, D.E., Guan, B., DeFlorio, M.J., Ralph, F.M. and Swain, D.L., 2020. Ridging associated with drought across the western and southwestern United States: Characteristics, trends, and predictability sources. *J. Climate*, *33*(7), 2485-2508. https://doi.org/10.1175/JCLI-D-19-0439.1

Gibson, P.B., Chapman, W.E., Altinok, A., Delle Monache, L., DeFlorio, M.J. and Waliser, D.E., 2021. Training machine learning models on climate model output yields skillful interpretable seasonal precipitation forecasts. *Communications Earth & Environment*, *2*(1), 159. https://doi.org/10.1038/s43247-021-00225-4

Hartmann, D.L., 2015. Pacific sea surface temperature and the winter of 2014. *Geophys. Res. Lett.*, *42*(6), 1894-1902. https://doi.org/10.1002/2015GL063083

Henderson, S.A., Maloney, E.D. and Barnes, E.A., 2016. The influence of the Madden–Julian oscillation on Northern Hemisphere winter blocking. *J. Climate*, *29*(12), 4597-4616. https://doi.org/10.1175/JCLI-D-15-0502.1

Henderson, S.A., Maloney, E.D. and Son, S.W., 2017. Madden–Julian oscillation Pacific teleconnections: The impact of the basic state and MJO representation in general circulation models. *J. Climate*, *30*(12), 4567-4587. https://doi.org/10.1175/JCLI-D-16-0789.1

Hersbach, H., Bell, B., Berrisford, P., Hirahara, S., Horányi, A., Muñoz-Sabater, J., Nicolas, J., Peubey, C., Radu, R., Schepers, D. and Simmons, A., 2020. The ERA5 global reanalysis. *Quart. J. of the Roy. Meteor. Society*, *146*(730), 1999-2049.

Horel, J. D., and J. M. Wallace, 1981: Planetary-scale atmospheric phenomena associated with the Southern Oscillation. *Mon. Wea. Rev.*, 109, 813–829, https://doi.org/10.1175/1520-0493(1981)109<0813:PSAPAW>2.0.CO;2.

Hoskins, B.J. and Ambrizzi, T., 1993. Rossby wave propagation on a realistic longitudinally varying flow. *J. Atmos. Sci., 50*(12), 1661-1671. https://doi.org/10.1175/1520-0469(1993)050<1661:RWPOAR>2.0.CO;2

Hoskins, B.J. and Karoly, D.J., 1981. The steady linear response of a spherical atmosphere to thermal and orographic forcing. *J. Atmos. Sci.*, *38*(6), 1179-1196. https://doi.org/10.1175/1520-0469(1981)038<1179:TSLROA>2.0.CO;2

Jiang, X., Waliser, D.E., Gibson, P.B., Chen, G. and Guan, W., 2022. Why Seasonal Prediction of California Winter Precipitation Is Challenging. *Bull. Amer. Meteor. Soc.*, *103*(12), E2688-E2700.

Jong, B.T., Ting, M. and Seager, R., 2016. El Niño's impact on California precipitation: Seasonality, regionality, and El Niño intensity. *Environmental Research Letters*, *11*(5), p.054021. https://doi.org/10.1088/1748-9326/11/5/054021

Kang, D., Kim, D., Ahn, M.S. and An, S.I., 2021. The role of the background meridional moisture gradient on the propagation of the MJO over the maritime continent. *J. Climate*, *34*(16), 6565-6581. https://doi.org/10.1175/JCLI-D-20-0085.1

Kirtman, B.P., Min, D., Infanti, J.M., Kinter, J.L., Paolino, D.A., Zhang, Q., Van Den Dool, H., Saha, S., Mendez, M.P., Becker, E. and Peng, P., 2014. The North Amer. multimodel ensemble: phase-1 seasonal-to-interannual prediction; phase-2 toward developing intraseasonal prediction. *Bull. Amer. Meteor. Soc.*, *95*(4), 585-601. https://doi.org/10.1175/BAMS-D-12-00050.1

Kumar, A. and Chen, M., 2020. Understanding skill of seasonal mean precipitation prediction over California during boreal winter and role of predictability limits. *J. Climate*, *33*(14), 6141-6163.https://doi.org/10.1175/JCLI-D-19-0275.1.

L'Heureux, M.L., Tippett, M.K. and Barnston, A.G., 2015. Characterizing ENSO coupled variability and its impact on North Amer. seasonal precipitation and temperature. *J. Climate*, *28*(10), 4231-4245. https://doi.org/10.1175/JCLI-D-14-00508.1.

Lau, N.C. and Nath, M.J., 1996. The role of the "atmospheric bridge" in linking tropical Pacific ENSO events to extratropical SST anomalies. *J. Climate*, *9*(9), 2036-2057. https://doi.org/10.1175/1520-0442(1996)009<2036:TROTBI>2.0.CO;2

Lee, M.Y., Hong, C.C. and Hsu, H.H., 2015. Compounding effects of warm sea surface temperature and reduced sea ice on the extreme circulation over the extratropical North Pacific and North America during the 2013–2014 boreal winter. *Geophys. Res. Lett.*, *42*(5), 1612-1618. https://doi.org/10.1002/2014GL062956

Lee, S.K., Lopez, H., Chung, E.S., DiNezio, P., Yeh, S.W. and Wittenberg, A.T., 2018. On the fragile relationship between El Niño and California rainfall. *Geophys. Res. Lett.*, *45*(2), 907-915. https://doi.org/10.1002/2017GL076197

Li, X., Hu, Z.Z., Liang, P. and Zhu, J., 2019. Contrastive influence of ENSO and PNA on variability and predictability of North Amer. winter precipitation. *J. Climate*, *32*(19), 6271-6284. https://doi.org/10.1175/JCLI-D-19-0033.1

Lim, Y., Peings, Y. and Magnusdottir, G., 2021. The role of atmospheric drivers in a sudden transition of California precipitation in the 2012/13 winter. *J. Geophys. Res.: Atmos.*, *126*(22), p.e2021JD035028. https://doi.org/10.1029/2021JD035028

Liu, F., Zhou, L., Ling, J., Fu, X. and Huang, G., 2016. Relationship between SST anomalies and the intensity of intraseasonal variability. *Theoretical and Applied Climatology*, *124*, 847-854. https://doi.org/10.1007/s00704-015-1458-2

Lopez, H. and Kirtman, B.P., 2019. ENSO influence over the Pacific North Amer. sector: Uncertainty due to atmospheric internal variability. *Climate dynamics*, *52*(9-10), 6149-6172. https://doi.org/10.1007/s00382-018-4500-0

Lorenz, E.N., 1963. Deterministic nonperiodic flow. *J. Atmos. Sci.*, *20*(2), 130-141. https://doi.org/10.1175/1520-0469(1963)020<0130:DNF>2.0.CO;2

Lund, J., Medellin-Azuara, J., Durand, J. and Stone, K., 2018. Lessons from California's 2012–2016 drought. *Journal of Water Resources Planning and Management*, *144*(10), p.04018067.

Maloney, E.D., Adames, Á.F. and Bui, H.X., 2019. Madden–Julian oscillation changes under anthropogenic warming. *Nature Climate Change*, *9*(1), 26-33. https://doi.org/10.1038/s41558-018-0331-6

Moon, J.Y., Wang, B. and Ha, K.J., 2011. ENSO regulation of MJO teleconnection. *Climate Dynamics*, *37*, 1133-1149. https://doi.org/10.1007/s00382-010-0902-3

Mundhenk, B.D., Barnes, E.A., Maloney, E.D. and Nardi, K.M., 2016. Modulation of atmospheric rivers near Alaska and the US West Coast by northeast Pacific height anomalies. *J. Geophys. Res.: Atmos.*, *121*(21), 12-751. https://doi.org/10.1002/2016JD025350

Mundhenk, B.D., Barnes, E.A., Maloney, E.D. and Baggett, C.F., 2018. Skillful empirical subseasonal prediction of landfalling atmospheric river activity using the Madden–Julian oscillation and quasi-biennial oscillation. *NPJ Climate and Atmospheric Science*, *1*(1), p.20177. https://doi.org/10.1038/s41612-017-0008-2

Patricola, C.M., O'Brien, J.P., Risser, M.D., Rhoades, A.M., O'Brien, T.A., Ullrich, P.A., Stone, D.A. and Collins, W.D., 2020. Maximizing ENSO as a source of western US hydroclimate predictability. *Climate Dynamics*, *54*, 351-372. https://doi.org/10.1007/s00382-019-05004-8.

Payne, A.E. and Magnusdottir, G., 2014. Dynamics of landfalling atmospheric rivers over the North Pacific in 30 years of MERRA reanalysis. *J. Climate*, *27*(18), 7133-7150. https://doi.org/10.1175/JCLI-D-14-00034.1

Payne, A.E. and Magnusdottir, G., 2016. Persistent landfalling atmospheric rivers over the west coast of North America. *Journal of Geophysical Research: Atmospheres*, *121*(22), 13-287. https://doi.org/10.1002/2016JD025549

Pedregosa, F., Varoquaux, G., Gramfort, A., Michel, V., Thirion, B., Grisel, O., Blondel, M., Prettenhofer, P., Weiss, R., Dubourg, V. and Vanderplas, J., 2011. Scikit-learn: Machine learning in Python. *the Journal of machine Learning research*, *12*, 2825-2830.

Peng, P., Kumar, A., Chen, M., Hu, Z.Z. and Jha, B., 2019. Was the North Amer. extreme climate in winter 2013/14 a SST forced response?. *Climate Dynamics*, *52*, 3099-3110. https://doi.org/10.1007/s00382-018-4314-0.

Peings, Y., Lim, Y. and Magnusdottir, G., 2022. Potential predictability of southwest US rainfall: Role of tropical and high-latitude variability. *J. Climate*, *35*(6), 1697-1717. https://doi.org/10.1175/JCLI-D-21-0775.1

Ralph, F.M. and Dettinger, M.D., 2011. Storms, floods, and the science of atmospheric rivers. *Eos, Transactions Amer. Geophysical Union*, *92*(32), 265-266. https://doi.org/10.1029/2011EO320001

Riddle, E.E., Stoner, M.B., Johnson, N.C., L'Heureux, M.L., Collins, D.C. and Feldstein, S.B., 2013. The impact of the MJO on clusters of wintertime circulation anomalies over the North Amer. region. *Climate Dynamics*, *40*, 1749-1766. https://doi.org/10.1007/s00382-012-1493-y

Rodgers, K.B., Lee, S.S., Rosenbloom, N., Timmermann, A., Danabasoglu, G., Deser, C., Edwards, J., Kim, J.E., Simpson, I.R., Stein, K. and Stuecker, M.F., 2021. Ubiquity of human-induced changes in climate variability. *Earth System Dynamics*, *12*(4), 1393-1411. https://doi.org/10.5194/esd-12-1393-2021

Ropelewski, C.F. and Halpert, M.S., 1986. North Amer. precipitation and temperature patterns associated with the El Niño/Southern Oscillation (ENSO). *Mon. Wea. Rev.*, *114*(12), 2352-2362. https://doi.org/10.1175/1520-0493(1986)114<2352:NAPATP>2.0.CO;2

Roundy, P.E., MacRitchie, K., Asuma, J. and Melino, T., 2010. Modulation of the global atmospheric circulation by combined activity in the Madden–Julian oscillation and the El Niño–Southern Oscillation during boreal winter. *J. Climate*, *23*(15), 4045-4059. https://doi.org/10.1175/2010JCLI3446.1

Roy, T., He, X., Lin, P., Beck, H.E., Castro, C. and Wood, E.F., 2020. Global evaluation of seasonal precipitation and temperature forecasts from NMME. *J. Hydrometeor.*, *21*(11), 2473-2486. https://doi.org/10.1175/JHM-D-19-0095.1

Rutz, J.J., Steenburgh, W.J. and Ralph, F.M., 2014. Climatological characteristics of atmospheric rivers and their inland penetration over the western United States. *Monthly Wea. Quart. Review*, *142*(2), 905-921. https://doi.org/10.1175/MWR-D-13-00168.1

Sardeshmukh, P.D. and Hoskins, B.J., 1988. The generation of global rotational flow by steady idealized tropical divergence. *J. Atmos. Sci*, *45*(7), 1228-1251. https://doi.org/10.1175/1520-0469(1988)045<1228:TGOGRF>2.0.CO;2

Seager, R. and Henderson, N., 2016. On the role of tropical ocean forcing of the persistent North Amer. west coast ridge of winter 2013/14. *J. Climate*, *29*(22), 8027-8049. https://doi.org/10.1175/JCLI-D-16-0145.1

Sengupta, A., Singh, B., DeFlorio, M. J., Raymond, C., Robertson, A. W., Zeng, X., Waliser D.E. and Jones, J. 2022. Advances in Subseasonal to Seasonal Prediction Relevant to

Water Management in the Western United States. *Bull. Amer. Meteor. Soc.*, 103(10), E2168-E2175. https://doi.org/10.1175/BAMS-D-22-0146.1

Siler, N., Kosaka, Y., Xie, S.P. and Li, X., 2017. Tropical ocean contributions to California's surprisingly dry El Niño of 2015/16. *J. Climate*, *30*(24), 10067-10079. https://doi.org/10.1175/JCLI-D-17-0177.1

Stan, C., Zheng, C., Chang, E.K.M., Domeisen, D.I.V., Garfinkel, C.I., Jenney, A.M., Kim, H., Lim, Y.K., Lin, H., Robertson, A. and Schwartz, C., 2022. Advances in the Prediction of MJO Teleconnections in the S2S Forecast Systems, *Bull. Amer. Meteor. Soc.*, 103(6), E1426–E1447. https://doi.org/10.1175/BAMS-D-21-0130.1

Swain, D.L., Tsiang, M., Haugen, M., Singh, D., Charland, A., Rajaratnam, B. and Diffenbaugh, N.S., 2014. The extraordinary California drought of 2013/2014: Character, context, and the role of climate change. *Bull. Amer. Meteor. Soc.*, *95*(9), p.S3.

Swain, D.L., 2015. A tale of two California droughts: Lessons amidst record warmth and dryness in a region of complex physical and human geography. *Geophys. Res. Lett.*, *42*(22), 9999-10. https://doi.org/10.1002/2015GL066628

Swain, D.L., Singh, D., Horton, D.E., Mankin, J.S., Ballard, T.C. and Diffenbaugh, N.S., 2017. Remote linkages to anomalous winter atmospheric ridging over the northeastern Pacific. *J. Geophys. Res.: Atmos.*, *122*(22), 12-194. https://doi.org/10.1002/2017JD026575

Swenson, E.T., Straus, D.M., Snide, C.E. and al Fahad, A., 2019. The role of tropical heating and internal variability in the California response to the 2015/16 ENSO event. *J. Atmos. Sci.*, *76*(10), 3115-3128. https://doi.org/10.1175/JAS-D-19-0064.1

Teng, H. and Branstator, G., 2017. Causes of extreme ridges that induce California droughts. *J. Climate*, *30*(4), 1477-1492. https://doi.org/10.1175/JCLI-D-16-0524.1

Trenberth, K.E., 1997. The definition of el nino. *Bull. Amer. Meteor. Soc.*, *78*(12), 2771-2778. https://doi.org/10.1175/1520-0477(1997)078<2771:TDOENO>2.0.CO;2

Vitart, F., Ardilouze, C., Bonet, A., Brookshaw, A., Chen, M., Codorean, C., Déqué, M., Ferranti, L., Fucile, E., Fuentes, M. and Hendon, H., 2017. The subseasonal to seasonal (S2S) prediction project database. *Bull. Amer. Meteor. Soc.*, *98*(1), 163-173. https://doi.org/10.1175/BAMS-D-16-0017.1

Wang, J., Kim, H., Kim, D., Henderson, S.A., Stan, C. and Maloney, E.D., 2020. MJO teleconnections over the PNA region in climate models. Part II: Impacts of the MJO and basic state. *J. Climate*, *33*(12), pp.5081-5101. https://doi.org/10.1175/JCLI-D-19-0865.1

Wang, J., Kim, H. and DeFlorio, M.J., 2022. Future changes of PNA-like MJO teleconnections in CMIP6 models: Underlying mechanisms and uncertainty. *J. Climate*, *35*(11), 3459-3478. https://doi.org/10.1175/JCLI-D-21-0445.1

Wang, S.Y.S., Yoon, J.H., Becker, E. and Gillies, R., 2017. California from drought to deluge. *Nature Climate Change*, *7*(7), 465-468. https://doi.org/10.1038/nclimate3330

Watanabe, M. and Kimoto, M., 2000. Atmosphere-ocean thermal coupling in the North Atlantic: A positive feedback. *Quart. J. of the Roy. Meteor. Society*, *126*(570), 3343-3369. https://doi.org/10.1002/qj.49712657017

Watson, P.A., Weisheimer, A., Knight, J.R. and Palmer, T.N., 2016. The role of the tropical West Pacific in the extreme Northern Hemisphere winter of 2013/2014. *J. Geophys. Res.: Atmos.*, *121*(4), 1698-1714. https://doi.org/10.1002/2015JD024048

Woolnough, S.J., Vitart, F. and Balmaseda, M.A., 2007. The role of the ocean in the Madden–Julian Oscillation: Implications for MJO prediction. *Quart. J. of the Roy. Meteor. Society,133*(622), 117-128. https://doi.org/10.1002/qj.4

Zhang, C., 2005. Madden-julian oscillation. *Reviews of Geophysics*, *43*(2). https://doi.org/10.1029/2004RG000158

Zhang, T., Hoerling, M.P., Wolter, K., Eischeid, J., Cheng, L., Hoell, A., Perlwitz, J., Quan, X.W. and Barsugli, J., 2018. Predictability and prediction of Southern California rains during strong El Niño events: A focus on the failed 2016 winter rains. *J. Climate*, *31*(2), 555-574. https://doi.org/10.1175/JCLI-D-17-0396.1

Zhou, W., Yang, D., Xie, S.P. and Ma, J., 2020. Amplified Madden–Julian oscillation impacts in the Pacific–North America region. *Nature Climate Change*, *10*(7), 654-660. https://doi.org/10.1038/s41558-020-0814-0